

Generative modelling of multivariate geometric extremes using normalising flows

Lambert De Monte*, Raphaël Huser†, Ioannis Papastathopoulos*, and Jordan Richards*

Abstract

Leveraging the recently emerging geometric approach to multivariate extremes and the flexibility of normalising flows on the hypersphere, we propose a principled deep-learning-based methodology that enables accurate joint tail extrapolation in all directions. We exploit theoretical links between intrinsic model parameters defined as functions on hyperspheres to construct models ranging from high flexibility to parsimony, thereby enabling the efficient modelling of multivariate extremes displaying complex dependence structures in higher dimensions with reasonable sample sizes. We use the generative feature of normalising flows to perform fast probability estimation for arbitrary Borel risk regions via an efficient Monte Carlo integration scheme. The good properties of our estimators are demonstrated via a simulation study in up to ten dimensions. We apply our methodology to the analysis of low and high extremes of wind speeds. In particular, we find that our methodology enables probability estimation for non-trivial extreme events in relation to electricity production via wind turbines and reveals interesting structure in the underlying data.

Keywords: Deep learning, density modelling on hyperspheres, statistics of extremes, wind speed modelling

*School of Mathematics and Maxwell Institute for Mathematical Sciences, University of Edinburgh, Edinburgh, EH9 3FD, Scotland

†Statistics Program, CEMSE Division, King Abdullah University of Science and Technology (KAUST), Thuwal 23955-6900, Saudi Arabia

1 Introduction

1.1 Motivation and previous work

Extreme events, whether of environmental, biological, or financial nature, only to name a few examples, pose recurring risks. Accurate and reliable assessment of their frequency and intensity allows for better planning, mitigation, and adaptation efforts. The mathematical framework of extreme value theory provides a principled approach to characterise, assess, and quantify the risk of extreme events of possibly yet-unobserved magnitudes.

In many real-world applications, a useful and practical approach to modelling stochastic phenomena and their extremes is to frame the questions of interest in a multivariate setting. Encoding observables into a finite-dimensional random vector, interest lies in estimating the probability that a realisation from the random vector belongs to specific extremal subsets.

Early theoretical work on the geometric interpretation of multivariate extremes examined conditions under which scaled independent draws from the distribution of a random vector converge in probability onto compact limit sets with respect to the Hausdorff distance (Geffroy, 1958, 1959; Fisher, 1969; Davis et al., 1988; Kinoshita and Resnick, 1991). Geometric considerations have recently found renewed theoretical interest (Balkema et al., 2010; Balkema and Nolde, 2010, 2012; Nolde, 2014), with Nolde and Wadsworth (2022) showing that this general framework unifies existing multivariate extremes approaches.

This development led to new statistical inference methods adopting a radial-angular representation in which an extreme event is defined in terms of the magnitude of radii given their directions, and hence, enable extrapolation in all directions of the multivariate support of a random vector. In particular, Wadsworth and Campbell (2024) propose a parametric approach to model quantities linked with the limit set of a given random

vector. Papastathopoulos et al. (2025) build on the geometric framework by establishing the weak convergence of exceedances of suitably chosen sequences of functions defined on hyperspheres to a limit Poisson point process. Leveraging the likelihood of the limit process, they build a Bayesian statistical model relying on latent Gaussian processes which can pool information from the radii and the directions of observations to perform extreme event probability estimation and to extrapolate probability and return sets in dimensions 2 and 3. Majumder et al. (2025) adopt a Bayesian approach with Bézier splines to model the limit set. Murphy-Barltrop et al. (2024) extend this line of work via deep learning methods to perform inference for the limit set in up to 8 dimensions, but only enable probability estimation for unbounded hyperboxes laying entirely in a quadrant of \mathbb{R}^d . Campbell and Wadsworth (2024) propose a piecewise-linear representation in dimension up to 5.

Parallel work explores modelling the exceedances of high functional thresholds of the univariate radial variable given a direction using a generalised Pareto distribution, motivated by univariate theory; see, *e.g.*, Simpson and Tawn (2024a,b), and Mackay and Jonathan (2024). An active area of research relates to finding representations for the parameters of this model to enable statistical inference in higher dimensions (Murphy-Barltrop et al., 2024; Mackay et al., 2024). Although powerful, current approaches face limitations in terms of how the distribution of the directional variable is modelled. For instance, they either resort to sampling from the empirical distribution of the directional variables (Mackay et al., 2024) or do not model it at all (Murphy-Barltrop et al., 2024). Recent work involving generative deep learning methods to model the directional variable highlights the need for scalable models, see Lhaut et al. (2025) and Wessel et al. (2025).

In this paper, we adopt a deep learning methodology based on normalising flows within the geometric extremes framework. Normalising flows provide a flexible and principled

approach to density estimation and possess generative properties enabling efficient sampling from inferred target densities. A review of normalising flows methods can be found in Kobzyev et al. (2021), and for their application to density estimation, see Dinh et al. (2017) and Papamakarios et al. (2017, 2021). In an extreme value analysis context, normalising flows were used by Hickling and Prangle (2023) to model the marginal tails of a random vector, but not to model its dependence structure; Hu and Castro-Camilo (2025) adopted real-valued non-volume preserving flows to model multivariate generalised Pareto distributions (Rootzén and Tajvidi, 2006). While typically constructed for hyperrectangular subsets of the d -dimensional reals, normalising flows have also been implemented on spheres (Ng and Zammit-Mangion, 2024) and on hyperspheres and tori (Rezende et al., 2020), yet not in the context of multivariate extremes.

1.2 Contributions and paper structure

In this work, we exploit the geometric properties of structural model parameters to enable semi-parametric statistical inference in higher dimensions. In particular, using theoretically-justified links between model parameters, our methodology allows imposing structure on model parameters by minimising relevant composite loss functions. These new model formulations bridge parsimony and flexibility, thereby enabling statistical inference in various dimension settings for varying complexity of dependence structures.

Adopting the radial-angular representation for random vectors, we use normalising flows to model the possibly complex distribution of directions of extreme events and the unit-volume shape of more general positive functions not necessarily integrating to one. This yields a new approach to perform quantile regression on hyperspherical domains and to enforce theoretically-justified structure between the parameters of the proposed models.

Additionally, we leverage the generative property of normalising flows to enable fast sampling from the fitted models and accurate probability estimation for arbitrary Borel subsets of the d -dimensional reals via Monte Carlo integration.

The paper is organised as follows. In Section 2, we provide background on the geometric approach to multivariate extremes and formulate specific model structures bridging parsimony and flexibility based on asymptotically-justified arguments. In Section 3, we introduce normalising flows and describe the gradient descent procedure used to fit our models. We discuss model regularisation options to reduce over-fitting and increase out-of-sample generalisation, and detail our probability estimation procedure. In Section 4, we conduct a simulation study to demonstrate our model’s ability to extrapolate and estimate the probability of extreme events in dimensions up to 10. In Section 5, we apply our methodology to jointly model low and high extremes of wind speeds in the Pacific Northwest region of the United States and assess their impact on electricity production. Last, in Section 6, we highlight the benefits of our methodology and suggest possible avenues for future work.

2 A geometric approach to multivariate extremes

2.1 Notation and assumptions

To ensure clarity and consistency in the presentation, this section defines the notation that will be used throughout and states the fundamental assumptions underpinning our analysis.

Commonly used manifolds: We denote by $\mathbb{R}_{\geq 0} := [0, \infty)$ and $\mathbb{R}_{> 0} := (0, \infty)$ the positive and strictly positive reals, respectively; by \mathbb{R}^d the d -dimensional reals with $d \geq 2$; by $\mathbb{S}^{d-1} := \{\mathbf{x} \in \mathbb{R}^d : \|\mathbf{x}\| = 1\}$ the $(d-1)$ -sphere (or hypersphere) with Euclidean norm $\|\cdot\|$; by $\mathbb{C}^{d-1} := \mathbb{S}^1 \times (-1, 1)^{d-2}$ (for $d > 2$, and $\mathbb{C}^1 := \mathbb{S}^1$) the hypercylinder.

Line segments and half-lines: We denote by $[\mathbf{x} : \mathbf{y}] := \{(1-t)\mathbf{x} + t\mathbf{y} : t \in [0, 1]\} \subset \mathbb{R}^d$ the closed line segment between $\mathbf{x} \in \mathbb{R}^d$ and $\mathbf{y} \in \mathbb{R}^d$, and by $[\mathbf{x} : \mathbf{y}] := \{(1-t)\mathbf{x} + t\mathbf{y} : t \in \mathbb{R}_{\geq 0}\} \subset \mathbb{R}^d$ the half-line emanating from $\mathbf{x} \in \mathbb{R}^d$ and passing through $\mathbf{y} \in \mathbb{R}^d$.

Starshaped sets and star-bodies: A set $\mathcal{S} \subseteq \mathbb{R}^d$ is star-shaped if there exists a *kernel* subset $\text{Ker}(\mathcal{S}) \subseteq \mathcal{S}$ such that $\forall \mathbf{x} \in \text{Ker}(\mathcal{S})$ and $\forall \mathbf{y} \in \mathcal{S}$, $[\mathbf{x} : \mathbf{y}] \subseteq \mathcal{S}$. Further, \mathcal{S} belongs to the class of star-bodies, denoted $\mathcal{S} \in \star$, if it is a compact starshaped set and $\mathbf{0} \in \text{Ker}(\mathcal{S})$.

Radial functions of star-bodies: Any star-body $\mathcal{S} \in \star$ is in one-to-one correspondance with its radial function $r_{\mathcal{S}} : \mathbb{S}^{d-1} \rightarrow \mathbb{R}_{\geq 0}$ where $r_{\mathcal{S}}(\mathbf{w}) = \sup\{\lambda > 0 : \lambda\mathbf{w} \in \mathcal{S}\}$, and $\partial\mathcal{S} = \{r_{\mathcal{S}}(\mathbf{w})\mathbf{w} : \mathbf{w} \in \mathbb{S}^{d-1}\}$ is the boundary of \mathcal{S} . A point $\mathbf{x} \in \mathbb{R}^d$ belongs to the closure $\overline{\mathcal{S}}$ if $\|\mathbf{x}\| \leq r_{\overline{\mathcal{S}}}(\mathbf{x}/\|\mathbf{x}\|)$, and to the complement $(\overline{\mathcal{S}})' := \mathbb{R}^d \setminus \overline{\mathcal{S}}$ of $\overline{\mathcal{S}}$ if $\|\mathbf{x}\| > r_{\overline{\mathcal{S}}}(\mathbf{x}/\|\mathbf{x}\|)$.

Normalised functions: We denote by f any (normalised) function integrating to 1 on its domain. A function f is understood as a probability density function (PDF) if its subscript is a random variable and as a normalised radial function if its subscript is a star-body.

Star-bodies as model parameters: Model parameters which are positive and bounded functions defined on \mathbb{S}^{d-1} can be interpreted as radial functions of star-bodies, providing compact notation. A model parameter $\Sigma \in \star$ then has value $r_{\Sigma}(\mathbf{w})$ at $\mathbf{w} \in \mathbb{S}^{d-1}$.

Random variables: We write $\mathbf{X} \sim \mathbb{P}_{\mathbf{X}}$ for random vector $\mathbf{X} \in \mathbb{R}^d$ distributed according to a probability measure $\mathbb{P}_{\mathbf{X}}(\cdot) := \mathbb{P}(\mathbf{X} \in \cdot)$. Its cumulative distribution function (CDF) $F_{\mathbf{X}}$ is given by $F_{\mathbf{X}}(\mathbf{x}) = \mathbb{P}_{\mathbf{X}}((-\infty, x_1] \times \cdots \times (-\infty, x_d])$. A random variable $R \in \mathbb{R}$ has quantile function F_R^{-1} with $F_R^{-1}(q) = \inf\{r \in \mathbb{R}_{>0} : F_R(r) \geq q\}$. We assume throughout that $\mathbb{P}_{\mathbf{X}}$ admits a PDF $f_{\mathbf{X}}$ with respect to the Lebesgue measure on \mathbb{R}^d and has standard Laplace marginals—with CDF $F_X(x) = \{\exp(x)/2\}^{\mathbb{1}(x \leq 0)} \{1 - \exp(-x)/2\}^{\mathbb{1}(x > 0)}$. A random variable R is said to follow a generalised Pareto (GP) distribution if $F_R(r) = 1 - [1 + \xi r/\sigma]_+^{-1/\xi}$, for $[x]_+ = \max\{0, x\}$, $\sigma \in \mathbb{R}_{>0}$, and $\xi \in \mathbb{R}$, and a standard GP distribution if $\sigma = 1$.

2.2 Background

The geometric approach to multivariate extremes aims to characterise the behaviour and to infer the probability of extreme events of a random vector $\mathbf{X} \in \mathbb{R}^d$ through the consideration of star-bodies describing the extremal dependence structure of $\mathbb{P}_{\mathbf{X}}$. Adopting the practical assumption that $\mathbb{P}_{\mathbf{X}}$ admits a PDF $f_{\mathbf{X}}$ and has standard Laplace marginal distributions, it follows from the work of Nolde and Wadsworth (2022) that the scaled sample cloud $N_n := \{\mathbf{X}_i / \log(n/2) : i = 1, \dots, n\}$ —with \mathbf{X}_i 's drawn independently from $\mathbb{P}_{\mathbf{X}}$ —converges in probability onto a limit star-body $\mathcal{G} \subseteq [-1, 1]^d$ in the sense that the Hausdorff distance between N_n and \mathcal{G} converges to 0 in probability as $n \rightarrow \infty$. Interest in \mathcal{G} follows from the rich insight it provides into the extremal dependence structure of $\mathbb{P}_{\mathbf{X}}$ and from key connections established with known extreme-value frameworks and measures of extremal dependence. A sufficient condition on $f_{\mathbf{X}}$ for N_n to converge onto \mathcal{G} is that

$$-\frac{\log f_{\mathbf{X}}(t\mathbf{x}_t)}{t} \rightarrow g_{\mathcal{G}}(\mathbf{x}), \quad \mathbf{x}_t \rightarrow \mathbf{x}, \text{ as } t \rightarrow \infty, \quad \mathbf{x} \in \mathbb{R}^d, \quad (1)$$

for a continuous gauge function $g_{\mathcal{G}} : \mathbb{R}^d \rightarrow \mathbb{R}_{\geq 0}$. Then, $\mathcal{G} \in \star$ and it has radial function $r_{\mathcal{G}} : \mathbb{S}^{d-1} \rightarrow \mathbb{R}_{\geq 0}$ given by $r_{\mathcal{G}} = 1/g_{\mathcal{G}}$ (Nolde and Wadsworth, 2022). Below, we describe connections between the convergence in probability of sample clouds onto limit sets and a refined weak convergence of exceedances of threshold functionals to a limiting multivariate radial generalised Pareto (GP) distribution (Papastathopoulos et al., 2025).

Defining the radius R and the direction \mathbf{W} of \mathbf{X} through

$$(R, \mathbf{W}) = (\|\mathbf{X}\|, \mathbf{X}/\|\mathbf{X}\|) \in \mathbb{R}_{>0} \times \mathbb{S}^{d-1}, \quad \mathbf{X} \in \mathbb{R}^d \setminus \{\mathbf{0}\}, \quad (2)$$

allows for the specification of a quantile set $\mathcal{Q}_q \in \star$ defined via the q th quantile of the

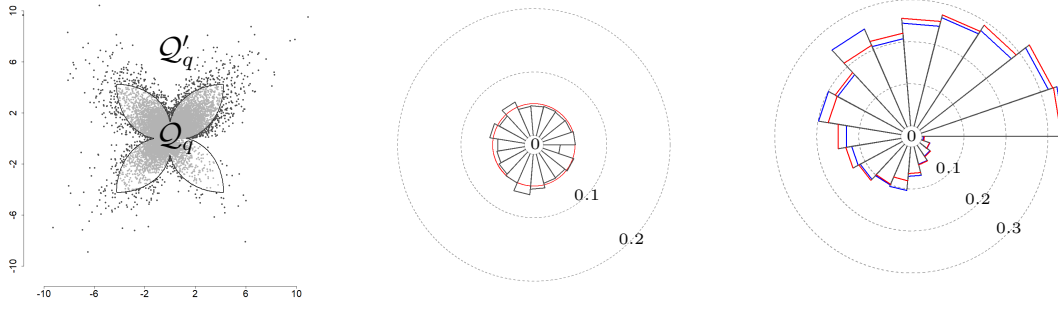


Figure 1: *Left*: Point cloud (dots) comprising 2×10^4 independent samples from a bivariate distribution having quantile set $\mathcal{Q}_{0.95}$, boundary $\partial\mathcal{Q}_{0.95}$ (solid black line) and complement $\mathcal{Q}'_{0.95}$. *Centre*: Empirical proportion of exceedances (lying in $\mathcal{Q}'_{0.95}$) binned by angular regions with true exceedance probability 0.05 (red). *Right*: Circular histogram of exceedance (blue) and of all sampled (red) directions. Concentric circles are density level sets.

conditional distribution of $R \mid \{\mathbf{W} = \mathbf{w}\}$. That is, \mathcal{Q}_q has radial function $r_{\mathcal{Q}_q} : \mathbb{S}^{d-1} \rightarrow \mathbb{R}_{\geq 0}$ where $r_{\mathcal{Q}_q}(\cdot) = F_{R|\mathbf{W}}^{-1}(q \mid \cdot)$. Papastathopoulos et al. (2025) show that for any $q \in (0, 1)$,

$$\mathbb{P}(R > r_{\mathcal{Q}_q}(\mathbf{W})) = \mathbb{P}(\mathbf{X} \in \mathcal{Q}'_q) = 1 - q \quad \text{and} \quad \{\mathbf{W} \mid R > r_{\mathcal{Q}_q}(\mathbf{W})\} \stackrel{d}{=} \mathbf{W}. \quad (3)$$

This is illustrated in Figure 1. Since $\mathbb{P}_{\mathbf{X}}$ admits a density by assumption, $\mathbb{P}_{\mathbf{W}}$ admits a density $f_{\mathbf{W}}$ with respect to the $(d-1)$ -dimensional spherical Lebesgue measure. Positivity of $f_{\mathbf{W}}$ on \mathbb{S}^{d-1} implies that it describes a set $\mathcal{W} \in \star$ with radial function $r_{\mathcal{W}} := f_{\mathbf{W}}$.

Further, Papastathopoulos et al. (2025) show conditions under which there exist a sequence of star-bodies, $\{\mathcal{G}_q \in \star : q \in (0, 1)\}$, and a function $\xi : \mathbb{S}^{d-1} \rightarrow \mathbb{R}$ such that

$$\left(H_{\mathbf{W}} \left(\frac{R - r_{\mathcal{Q}_q}(\mathbf{W})}{r_{\mathcal{G}_q}(\mathbf{W})} \right), \mathbf{W} \right) \mid \{R > r_{\mathcal{Q}_q}(\mathbf{W})\} \xrightarrow{d} (U, \mathbf{V}), \quad \text{as } q \rightarrow 1, \quad (4)$$

where $U \sim \text{Uniform}(0, 1)$, $\mathbf{V} \sim \mathbb{P}_{\mathbf{W}}$, and $H_{\mathbf{w}}$ denotes the CDF of a standard generalised Pareto (GP) distribution with shape $\xi(\mathbf{w})$. Convergence (4) implies a limiting distribution for which radial exceedances of \mathcal{Q}_q follow a GP distribution with scale \mathcal{G}_q and shape ξ varying along directions which are distributed according to $\mathbb{P}_{\mathbf{W}}$.

In the important case that \mathbf{X} has standard Laplace marginals, here satisfied by assumption, Papastathopoulos et al. (2025) show that if convergence (1) holds uniformly on \mathbb{S}^{d-1} , then that of (4) holds with $\mathcal{G}_q = \mathcal{G}$ independent of q and with $\xi \equiv 0$ —interpreted as $H_{\mathbf{w}}(z) = 1 - \exp(-z)$, $z \geq 0$, the exponential distribution. Extrapolation is enabled by assuming that the limiting distribution holds exactly above some fixed level $q \in (0, 1)$: we onwards assume that the excesses $\mathbf{X} \mid \{\mathbf{X} \notin \mathcal{Q}_q\}$ follow a multivariate radial exponential distribution with scaling set \mathcal{G} and directional set \mathcal{W} exactly—see Section S.1 of the Supplementary material for a definition. Then, for every Borel set $\mathcal{R} \subseteq \mathcal{Q}'_q$, the probability that a new draw from \mathbf{X} falls in \mathcal{R} is $\mathbb{P}[\mathbf{X} \in \mathcal{R}] = (1 - q)\mathbb{P}[\mathbf{X} \in \mathcal{R} \mid \mathbf{X} \in \mathcal{Q}'_q]$ where

$$\mathbb{P}[\mathbf{X} \in \mathcal{R} \mid \mathbf{X} \in \mathcal{Q}'_q] = \int_{\mathbb{S}^{d-1}} \int_{\rho([\mathbf{0}:\mathbf{w}) \cap \mathcal{R})} \frac{1}{r_{\mathcal{G}}(\mathbf{w})} \exp\left\{-\frac{r - r_{\mathcal{Q}_q}(\mathbf{w})}{r_{\mathcal{G}}(\mathbf{w})}\right\} f_{\mathbf{W}}(\mathbf{w}) dr d\mathbf{w}, \quad (5)$$

$\rho(\cdot) = \{\|\mathbf{x}\| : \mathbf{x} \in \cdot \subseteq \mathbb{R}^d\}$ and $[\mathbf{0} : \mathbf{w})$ denotes the half-line from $\mathbf{0}$ through $\mathbf{w} \in \mathbb{S}^{d-1}$.

Below, we detail theoretical links between the sets \mathcal{Q}_q , \mathcal{G} , and \mathcal{W} , and use them in the next Section 2.3 to specify new models. Firstly, Wadsworth and Campbell (2024) show that, under mild conditions, \mathcal{Q}_q is asymptotically a scale multiple of \mathcal{G} , that is,

$$\lim_{q \rightarrow 1} \frac{r_{\mathcal{Q}_q}(\mathbf{w})}{\alpha_q} = r_{\mathcal{G}}(\mathbf{w}), \quad \mathbf{w} \in \mathbb{S}^{d-1}, \quad (6)$$

where $\alpha_q = -\log(1 - q)\{1 + o(1)\}$. Secondly, while convergence (4) implies that \mathcal{G} intervenes in the limit density $f_{R|\{R > r_{\mathcal{Q}_q}(\mathbf{w}), \mathbf{w}\}}$, it may also more broadly impact the density of exceedances $f_{\mathbf{X}|\mathbf{X} \in \mathcal{Q}'_q}(r\mathbf{w}) = r^{d-1} f_{R|\{R > r_{\mathcal{Q}_q}(\mathbf{w}), \mathbf{w}\}}(r|\mathbf{w}) f_{\mathbf{W}}(\mathbf{w})$, for $r > 0$ and $\mathbf{w} \in \mathbb{S}^{d-1}$, via the directional variable \mathbf{W} . In particular, Papastathopoulos et al. (2025) show that if $f_{\mathbf{X}}$ is a composition of a decreasing, positive, and continuous function $h_0 : \mathbb{R}_{\geq 0} \rightarrow \mathbb{R}_{\geq 0}$ and of the inverse of a (-1) -homogeneous function $r_{\mathcal{G}} : \mathbb{R}^d \rightarrow \mathbb{R}_{\geq 0}$ describing the shape of a

set $\mathcal{G} \in \star$, that is, $f_{\mathbf{X}}(\mathbf{x}) = h_0(1/r_{\mathcal{G}}(\mathbf{x}))$, $\mathbf{x} \in \mathbb{R}^d$ —in which case $f_{\mathbf{X}}$ is homothetic with respect to $1/r_{\mathcal{G}}$ (Balkema and Nolde, 2010)—then \mathcal{G} and \mathcal{W} are indeed linked via

$$f_{\mathbf{W}}(\mathbf{w}) = \frac{r_{\mathcal{G}}(\mathbf{w})^d}{\int_{\mathbb{S}^{d-1}} r_{\mathcal{G}}(\mathbf{w})^d d\mathbf{w}}, \quad \mathbf{w} \in \mathbb{S}^{d-1}. \quad (7)$$

Papastathopoulos et al. (2025) show, for known families of distributions and real data settings, that the use of observed directions may reduce the uncertainty in estimates of \mathcal{G} .

2.3 Proposed models

Building upon Section 2.2, we propose models bridging flexibility and parsimony to capture complex dependence structures in low dimensions and to extend semi-parametric estimation to higher dimensions by imposing structure on the parameters \mathcal{Q}_q , \mathcal{G} , and \mathcal{W} .

We first define a base model, M_0 , assuming no shared structure between the parameters \mathcal{Q}_q , \mathcal{G} , and \mathcal{W} , which can thus have arbitrarily differing geometries. Among all models proposed below, M_0 can capture the widest range of dependence structures and is thus considered the most flexible. A visual representation of all model structures is given in Figure 2; their specific parameterisations are given in Table 1.

To specify more parsimonious models, we leverage theoretical results from Section 2.2 to motivate links between the geometries of the three set parameters. Concretely, we say that two sets $\mathcal{B}_1, \mathcal{B}_2 \in \star$ with radial functions $r_{\mathcal{B}_1}$ and $r_{\mathcal{B}_2}$ are linked if there exists a bijection $\psi : \mathbb{R}_{\geq 0} \rightarrow \mathbb{R}_{\geq 0}$ such that $r_{\mathcal{B}_1} = \psi \circ r_{\mathcal{B}_2}$. Without loss and for identifiability purposes, we use the fact that the radial function of any set $\mathcal{B} \in \star$ can be written as $r_{\mathcal{B}} = \beta_{\mathcal{B}} f_{\mathcal{B}}$ for some scalar $\beta_{\mathcal{B}} > 0$ and shape function $f_{\mathcal{B}} : \mathbb{S}^{d-1} \rightarrow \mathbb{R}_{\geq 0}$ integrating to one. Also, we use that for any $\mathcal{B}_1, \mathcal{B}_2 \in \star$ with $r_{\mathcal{B}_1} > 0$ and $r_{\mathcal{B}_2}$, there exists a deformation set \mathcal{D} with radial function $r_{\mathcal{D}} = \beta_{\mathcal{D}} f_{\mathcal{D}} = r_{\mathcal{B}_2}/r_{\mathcal{B}_1}$ such that $r_{\mathcal{B}_2} = r_{\mathcal{D}} r_{\mathcal{B}_1}$, for $\beta_{\mathcal{D}} > 0$ and $f_{\mathcal{D}} : \mathbb{S}^{d-1} \rightarrow \mathbb{R}_{\geq 0}$ integrating

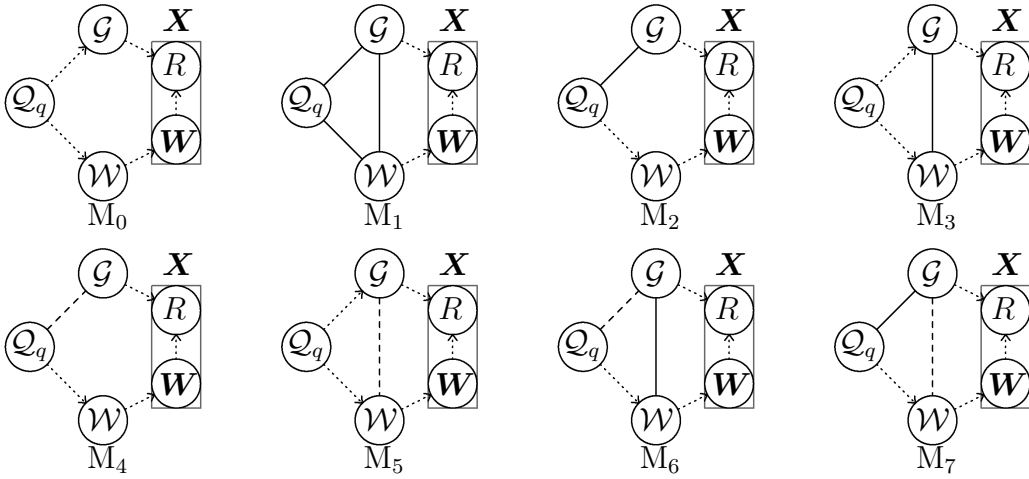


Figure 2: Structures of the fully decoupled model M_0 , the homothetic model M_1 , the intermediate models M_2 and M_3 , and the constrained models M_4 to M_7 . Solid edges imply an exact link between parameters. Dashed edges imply penalisation from departure of equalities (6) or (7). Dotted arrows imply independence in parameter construction.

Table 1: Parameter specification of models M_0 to M_7 for scalars $\beta_{Q_q}, \beta_G > 0$, shapes $f_{Q_q}, f_G, f_D : \mathbb{S}^{d-1} \rightarrow \mathbb{R}_{\geq 0}$, and PDF of directions $f_W : \mathbb{S}^{d-1} \rightarrow \mathbb{R}_{\geq 0}$.

Parameter	M_0	M_1	M_2	M_3	M_4	M_5	M_6	M_7
r_{Q_q}	$\beta_{Q_q} f_{Q_q}$	$\beta_{Q_q} f_W^{\frac{1}{d}}$	$\beta_{Q_q} f_G$	$\beta_{Q_q} f_{Q_q}$	$\beta_{Q_q} f_{Q_q}$	$\beta_{Q_q} f_D f_G$	$\beta_{Q_q} (f_D f_W)^{\frac{1}{d}}$	$\beta_{Q_q} (f_D f_W)^{\frac{1}{d}}$
r_G	$\beta_G f_G$	$\beta_G f_W^{\frac{1}{d}}$	$\beta_G f_G$	$\beta_G f_W^{\frac{1}{d}}$	$\beta_G (f_D f_W)^{\frac{1}{d}}$	$\beta_G f_G$	$\beta_G f_W^{\frac{1}{d}}$	$\beta_G (f_D f_W)^{\frac{1}{d}}$

to one. Then, \mathcal{B}_2 has radial function $r_{\mathcal{B}_2} = \beta_{\mathcal{B}_2} f_D f_{\mathcal{B}_1}$ with $\beta_{\mathcal{B}_2} = \beta_D \beta_{\mathcal{B}_1} > 0$. Note that if the shape f_D is constant, $\beta_{\mathcal{B}_2} f_D$ is constant and \mathcal{B}_1 and \mathcal{B}_2 have the same shape.

Therefore, whenever $f_G, f_W > 0$, we can express Q_q and G in terms of G and W , via

$$r_{Q_q}(\mathbf{w}) = \beta_{Q_q} f_{D_1}(\mathbf{w}) f_G(\mathbf{w}) \quad \text{and} \quad r_G(\mathbf{w}) = \beta_G \{f_{D_2}(\mathbf{w}) f_W(\mathbf{w})\}^{1/d}, \quad \mathbf{w} \in \mathbb{S}^{d-1}, \quad (8)$$

where f_{D_1}, f_{D_2} are respectively the shapes of deformation sets $\mathcal{D}_1, \mathcal{D}_2 \in \star$, and $\beta_{Q_q}, \beta_G > 0$.

We specify our most parsimonious model, labelled M_1 , by setting f_{D_1} and f_{D_2} constant on \mathbb{S}^{d-1} . This corresponds to assuming that, at a fixed probability level $q \in (0, 1)$ and above, Q_q is exactly a scale multiple of G —that is, $r_{Q_q} \propto r_G$, a practical version of as-

sumption (6)—and that assumption (7) holds exactly. For model M_1 , the shapes of \mathcal{Q}_q , \mathcal{G} , and \mathcal{W} are thus described by a single shape function $f_{\mathbf{W}}$.

Two models arise from assuming that only one of results (6) and (7) holds exactly for \mathbf{X} above a finite probability level $q \in (0, 1)$. These models, M_2 and M_3 , correspond to one of \mathcal{D}_1 or \mathcal{D}_2 having constant shape, thus linking two parameters via a single shape. The remaining parameter, either \mathcal{Q}_q or \mathcal{W} , then has independent shape $f_{\mathcal{Q}_q}$ or $f_{\mathbf{W}}$, respectively.

A third set of models, M_4 to M_7 , arises by weakening the exact link between pairs of parameters and constraining them from deviating too much from each other. They are defined using parameterisation (8) with non-constant sets \mathcal{D}_1 or \mathcal{D}_2 —denoted by dashed edges in Figure 2—with deformation shapes penalised for departure from a uniform shape. Concretely, M_4 bridges M_0 and M_2 ; M_5 bridges M_0 and M_3 ; M_6 bridges M_1 and M_3 ; M_7 bridges M_1 and M_2 . Details on penalisation are deferred to Section S.4.

3 Statistical inference

3.1 Marginal model and transformation to Laplace margins

Let $\underline{\mathbf{x}}^\circ = \{\mathbf{x}_i^\circ = (x_{i,1}^\circ, \dots, x_{i,d}^\circ) \in \mathbb{R}^d : i = 1, \dots, n\}$ be draws from a distribution $\mathbb{P}_{\mathbf{X}^\circ}$ whose marginals $F_{X_j^\circ}$, $j = 1, \dots, d$, do not necessarily follow the standard Laplace CDF denoted by F_L . We transform $\underline{\mathbf{x}}^\circ$ to $\underline{\mathbf{x}} := \{\mathbf{x}_i = (\hat{\varphi}_j(x_{i,j}^\circ) : j = 1, \dots, d) : i = 1, \dots, n\}$ via the inverse Laplace and approximate probability integral transforms $\hat{\varphi}_j = F_L^{-1} \circ \hat{F}_{X_j^\circ}$, where

$$\hat{F}_{X_j^\circ}(x) = \begin{cases} \left[1 - \left\{ 1 - \hat{\xi}_{j,-} \left(\frac{x - u_{j,-}}{\hat{\sigma}_{j,-}} \right) \right\}_+^{-1/\hat{\xi}_{j,-}} \right] \tilde{F}_j(u_{j,-}), & x \leq u_{j,-} \\ \tilde{F}_j(x), & u_{j,-} < x \leq u_{j,+} \\ 1 - [1 - \tilde{F}_j(u_{j,+})] \left\{ 1 + \hat{\xi}_{j,+} \left(\frac{x - u_{j,+}}{\hat{\sigma}_{j,+}} \right) \right\}_+^{-1/\hat{\xi}_{j,+}}, & x > u_{j,+} \end{cases}, \quad (9)$$

is an estimate of F_{X_j} , with $\tilde{F}_j(\cdot) = (n+1)^{-1} \sum_{i=1}^n \mathbb{1}[x_{i,j}^o \leq \cdot]$ the empirical distribution function of the j th margin, and with $(\hat{\sigma}_{j,-}, \hat{\xi}_{j,-})$ and $(\hat{\sigma}_{j,+}, \hat{\xi}_{j,+})$ the estimated scale and shape parameters of the GP distribution for the lower and upper tail fitted to the j^{th} margin below and above low and high thresholds $u_{j,-}$ and $u_{j,+}$, respectively.

As a result, $\underline{\mathbf{x}}$ has approximate standard Laplace margins.

3.2 Deep learning of PDFs and positive functions on \mathbb{S}^{d-1}

In this section, we detail a method based on normalising flows to infer PDFs and positive functions defined almost everywhere (*a.e.*) on \mathbb{S}^{d-1} to parameterise the models of Section 2.

Formally, a normalising flow is a diffeomorphism—a differentiable function with differentiable inverse—mapping a base distribution to a target distribution. If \mathbf{Y} and \mathbf{Z} are random variables on probability spaces $(\mathcal{Y}, \mathcal{F}_{\mathcal{Y}}, \mathbb{P}_{\mathbf{Y}})$ and $(\mathcal{Z}, \mathcal{F}_{\mathcal{Z}}, \mathbb{P}_{\mathbf{Z}})$ and admit target and base PDFs $f_{\mathbf{Y}}$ and $f_{\mathbf{Z}}$, respectively, the transformation of $f_{\mathbf{Z}}$ by a normalising flow h yields

$$f_{\mathbf{Y}}(\mathbf{y}) = f_{\mathbf{Z}}\{h^{-1}(\mathbf{y})\} \left| \frac{\partial h^{-1}(\mathbf{y})}{\partial \mathbf{y}} \right|, \quad \mathbf{y} \in \mathcal{Y}, \quad (10)$$

where $|\partial h^{-1}(\mathbf{y})/\partial \mathbf{y}|$ is the Jacobian determinant of h . In practice, $h = h_k \circ \dots \circ h_1$ is usually taken to be a deep composition of k simple diffeomorphisms h_1, \dots, h_k with tractable Jacobians, thereby enabling flexible transformations of the base PDF $f_{\mathbf{Z}}$. Details about the normalising flow constructions are provided in Section S.2. Below, we introduce the method proposed by Rezende et al. (2020) to infer a PDF *a.e.* on the hypersphere.

The approach consists in translating the problem of learning a PDF *a.e.* on the unit hypersphere \mathbb{S}^{d-1} to that of learning it on the hypercylinder $\mathbb{C}^{d-1} := \mathbb{S}^1 \times (-1, 1)^{d-2}$, for

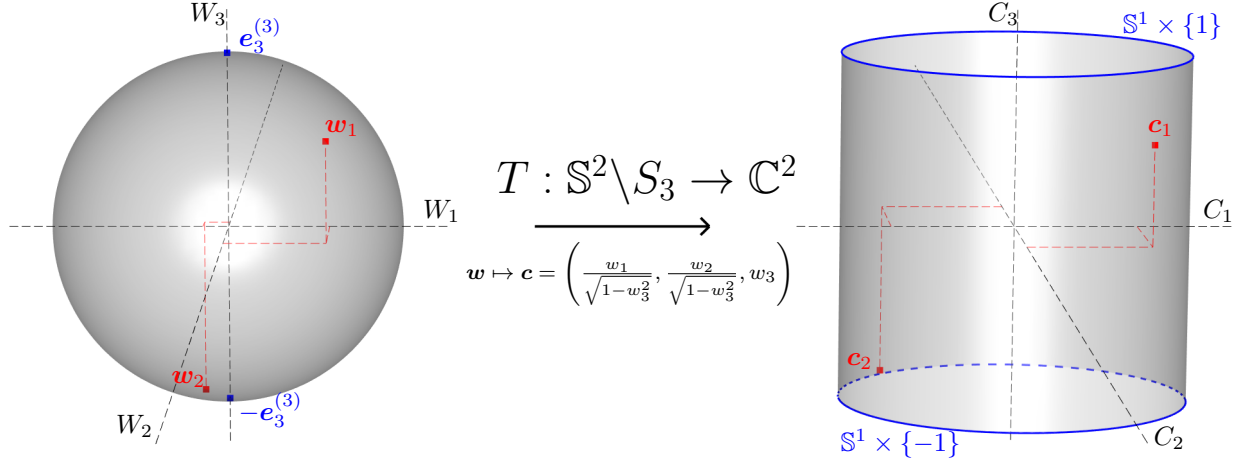


Figure 3: Visualisation of the map $T : \mathbb{S}^{d-1} \setminus S_d \rightarrow \mathbb{C}^{d-1}$ for the case $d = 3$. The directions $\mathbf{w}_1, \mathbf{w}_2 \in \mathbb{S}^2 \setminus S_3 = \mathbb{S}^2 \setminus \{\pm \mathbf{e}_3^{(3)}\}$ are mapped to $\mathbf{c}_1 = T(\mathbf{w}_1), \mathbf{c}_2 = T(\mathbf{w}_2) \in \mathbb{C}^2 = \mathbb{S}^1 \times (-1, 1)$.

$d \geq 2$, through a recursive, deterministic, and reversible map (detailed in Section S.3),

$$T : \mathbb{S}^{d-1} \setminus S_d \rightarrow \mathbb{C}^{d-1}, \quad (11)$$

where $S_d := \{\pm \mathbf{e}_d^{(3)}, \dots, \pm \mathbf{e}_d^{(d)}\}$ is the set of singularities at which the map (11) is undefined, and where $\mathbf{e}_n^{(m)}$ denotes the vector of size n whose sole non-zero m th component is equal to 1. Figure 3 illustrates the map T in the case $d = 3$ and the two singularities S_3 of the sphere \mathbb{S}^2 which are mapped to the boundaries $\mathbb{S}^1 \times \{-1\}$ and $\mathbb{S}^1 \times \{1\}$ of the cylinder \mathbb{C}^2 . Since S_d has finite cardinality $\#S_d = 2(d-2)$, it has measure 0 with respect to any measure that is absolutely continuous with respect to the spherical Lebesgue measure on \mathbb{S}^{d-1} .

It follows from the map (11) that a target PDF $f_{\mathcal{B}} : \mathbb{S}^{d-1} \setminus S_d \rightarrow \mathbb{R}_{\geq 0}$, describing the shape of a star-body $\mathcal{B} \in \mathbb{R}^d$ a.e., can be written as $f_{\mathcal{B}}(\mathbf{w}) = f_{\mathbf{Y}}(T(\mathbf{w})) |\partial T(\mathbf{w}) / \partial \mathbf{w}|$ for $\mathbf{w} \in \mathbb{S}^{d-1} \setminus S_d$ and a PDF $f_{\mathbf{Y}}$ on \mathbb{C}^{d-1} . Using expression (10), $f_{\mathcal{B}}$ can in turn be modelled in terms of a known base PDF $f_{\mathbf{Z}} : \mathbb{C}^{d-1} \rightarrow \mathbb{R}_{\geq 0}$ and a normalising flow $h_{\mathcal{B}}$ as

$$f_{\mathcal{B}}(\mathbf{w}) = f_{\mathbf{Z}}\{h_{\mathcal{B}}^{-1}(T(\mathbf{w}))\} \left| \frac{\partial h_{\mathcal{B}}^{-1}(T(\mathbf{w}))}{\partial T(\mathbf{w})} \right| \left| \frac{\partial T(\mathbf{w})}{\partial \mathbf{w}} \right|, \quad \mathbf{w} \in \mathbb{S}^{d-1} \setminus S_d, \quad (12)$$

with Jacobian determinant $|\partial T(\mathbf{w})/\mathbf{w}|$ given in Section S.3.

Equation (12) provides a model for $f_{\mathbf{W}}$ —by replacing \mathcal{B} with \mathcal{W} —which relies on learning the normalising flow $h_{\mathcal{W}}$. Further, a model for the radial function $r_{\mathcal{B}}$ of a general starshaped set \mathcal{B} —such as \mathcal{Q}_q or \mathcal{G} —can be obtained via $r_{\mathcal{B}} = \beta_{\mathcal{B}} f_{\mathcal{B}}$ where $f_{\mathcal{B}}$ is as in model (12), and $\beta_{\mathcal{B}} > 0$ is a coefficient to be learned alongside the normalising flow $h_{\mathcal{B}}$.

The invertibility of normalising flows enables efficient sampling from a target density $f_{\mathcal{B}}$ via $T^{-1}(h_{\mathcal{B}}(\mathbf{Z}))$ for $\mathbf{Z} \sim f_{\mathbf{Z}}$. Since $\mathbf{Z} \in \mathbb{C}^{d-1}$, a natural base density is the uniform density on \mathbb{C}^{d-1} . Since \mathbf{W} admits a spherical Lebesgue density by assumption, $\mathbb{P}_{\mathbf{W}}(S^d) = 0$ and it does not matter that there is no $\mathbf{c} \in \mathbb{C}^{d-1}$ such that $T^{-1}(h_{\mathcal{W}}(\mathbf{c})) \in S^d$.

3.3 Statistical inference via loss minimisation

To implement the models discussed in Section 2.3, we use the deep-learning-based methodology described in Section 3.2 and rely on the *normflows* package (Stimper et al., 2023), a *PyTorch* (Paszke et al., 2019) implementation of normalising flows via the Python programming language. Below, we describe a gradient descent approach to model fitting.

Model M_0 : Model M_0 can be fitted by sequentially obtaining estimates for the parameters \mathcal{Q}_q , \mathcal{G} , and \mathcal{W} , for fixed $q \in (0, 1)$. To obtain an estimate of \mathcal{Q}_q , say $\hat{\mathcal{Q}}_q$, we seek the estimates $\hat{\beta}_{\mathcal{Q}_q}$ and $\hat{f}_{\mathcal{Q}_q}$ minimising the quantile loss (Koenker and Bassett, 1978), *i.e.*, $(\hat{\beta}_{\mathcal{Q}_q}, \hat{f}_{\mathcal{Q}_q}) = \operatorname{argmin}_{(\beta_{\mathcal{Q}_q}, f_{\mathcal{Q}_q})} \mathcal{L}_{\mathcal{Q}_q}(\beta_{\mathcal{Q}_q}, f_{\mathcal{Q}_q}; \underline{\mathbf{x}})$ where, for $z_i = \|\mathbf{x}_i\| - \beta_{\mathcal{Q}_q} f_{\mathcal{Q}_q}(\mathbf{x}_i / \|\mathbf{x}_i\|)$,

$$\mathcal{L}_{\mathcal{Q}_q}(\beta_{\mathcal{Q}_q}, f_{\mathcal{Q}_q}; \underline{\mathbf{x}}) = \frac{1}{n} \sum_{i=1}^n \max \{ (1 - q)z_i, qz_i \}. \quad (13)$$

We minimise $\mathcal{L}_{\mathcal{Q}_q}$ via an iterative gradient descent approach consisting in a two-step procedure: for each gradient descent step $j \in \{1, \dots, m\}$, we first minimise $\mathcal{L}_{\mathcal{Q}_q}$ with respect

to $\beta_{\mathcal{Q}_q}$ conditionally on the shape $\hat{f}_{\mathcal{Q}_q}^{(j-1)}$ (at step $j-1$) resulting in an estimate $\hat{\beta}_{\mathcal{Q}_q}^{(j)}$, and then evaluate the gradient of $\mathcal{L}_{\mathcal{Q}_q}$ at $(\hat{\beta}_{\mathcal{Q}_q}^{(j)}, \hat{f}_{\mathcal{Q}_q}^{(j-1)})$ to perform a descent step modifying the flow $h_{\mathcal{Q}_q}$ associated with $\hat{f}_{\mathcal{Q}_q}$ conditionally on $\hat{\beta}_{\mathcal{Q}_q}^{(j)}$, resulting in an estimate $\hat{f}_{\mathcal{Q}_q}^{(j)}$. The minimiser $(\hat{\beta}_{\mathcal{Q}_q}, \hat{f}_{\mathcal{Q}_q})$ is used to form $\hat{\mathcal{Q}}_q$ via its radial function $r_{\hat{\mathcal{Q}}_q} = \hat{\beta}_{\mathcal{Q}_q} \hat{f}_{\mathcal{Q}_q}$ and to define $\mathcal{E} := \{i \in \{1, \dots, n\} : \|\mathbf{x}_i\| > r_{\hat{\mathcal{Q}}_q}(\mathbf{x}_i/\|\mathbf{x}_i\|)\}$, the indices of exceedances of $\hat{\mathcal{Q}}_q$.

To infer \mathcal{G} , we again use a two-step minimisation procedure for $\beta_{\mathcal{G}}$ and $f_{\mathcal{G}}$, but with the mean negative log-likelihood of the conditional radial component, $R \mid \mathbf{W}$, as the loss:

$$\mathcal{L}_{\mathcal{G}}(\beta_{\mathcal{G}}, f_{\mathcal{G}}; r_{\hat{\mathcal{Q}}_q}, \underline{\mathbf{x}}) = -\frac{1}{\#\mathcal{E}} \sum_{i \in \mathcal{E}} \log \left[\left\{ \beta_{\mathcal{G}} f_{\mathcal{G}} \left(\frac{\mathbf{x}_i}{\|\mathbf{x}_i\|} \right) \right\}^{-1} \exp \left\{ -\frac{\|\mathbf{x}_i\| - r_{\hat{\mathcal{Q}}_q}(\mathbf{x}_i/\|\mathbf{x}_i\|)}{\beta_{\mathcal{G}} f_{\mathcal{G}}(\mathbf{x}_i/\|\mathbf{x}_i\|)} \right\} \right]. \quad (14)$$

We note that, conditionally on a shape $\hat{f}_{\mathcal{G}}^{(j-1)}$ at step $j-1$ of gradient descent, the minimiser $\hat{\beta}_{\mathcal{G}}^{(j)}$ is $\hat{\beta}_{\mathcal{G}}^{(j)} = (\#\mathcal{E})^{-1} \sum_{i \in \mathcal{E}} \{\|\mathbf{x}_i\| - r_{\hat{\mathcal{Q}}_q}(\mathbf{x}_i/\|\mathbf{x}_i\|)\} / \hat{f}_{\mathcal{G}}^{(j-1)}(\mathbf{x}_i/\|\mathbf{x}_i\|)$, the closed-form maximum likelihood estimate of the scale parameter $\beta_{\mathcal{G}}$, and is therefore fast to compute.

Finally, inferring the directional set \mathcal{W} is simpler as it solely requires minimising the loss $\mathcal{L}_{\mathcal{W}}$ chosen as the negative log-likelihood of the observed directions, that is,

$$\mathcal{L}_{\mathcal{W}}(f_{\mathcal{W}}; \mathcal{E}, \underline{\mathbf{x}}) = -\frac{1}{\#\mathcal{E}} \sum_{i \in \mathcal{E}} \log f_{\mathcal{W}}(\mathbf{x}_i/\|\mathbf{x}_i\|). \quad (15)$$

Owing to property (3), and assuming that \mathcal{Q}_q is well estimated by $\hat{\mathcal{Q}}_q$, we may use all observed directions $\{\mathbf{x}/\|\mathbf{x}\| : \mathbf{x} \in \underline{\mathbf{x}}\}$ to infer \mathcal{W} instead of only the exceedances of $\hat{\mathcal{Q}}_q$; in this case, the loss (15) can be modified by replacing \mathcal{E} with $\{1, \dots, n\}$. This proves useful as exceedance directions of $\hat{\mathcal{Q}}_q$ can be scarce for q near 1.

Model M₁: Since the negative losses $-\mathcal{L}_{\mathcal{G}}$ and $-\mathcal{L}_{\mathcal{W}}$ are mean log-likelihoods of radial exceedances $\{R - r_{\mathcal{Q}_q}(\mathbf{w})\} \mid \{R > r_{\mathcal{Q}_q}(\mathbf{w}), \mathbf{W} = \mathbf{w}\}$ and of directions of exceedance

$\mathbf{W} \mid \{R > r_{\mathcal{Q}_q}(\mathbf{W})\}$, respectively, their sum forms a valid mean log-likelihood for the pair $(R - r_{\mathcal{Q}_q}(\mathbf{W}), \mathbf{W}) \mid \{R > r_{\mathcal{Q}_q}(\mathbf{W})\}$. Hence, for fixed $q \in (0, 1)$, model M_1 can naturally be fitted by minimising the composite loss

$$\begin{aligned} \mathcal{L}_{\mathcal{Q}_q, \mathcal{G}, \mathcal{W}}(\beta_{\mathcal{Q}_q}, \beta_{\mathcal{G}}, f_{\mathbf{W}}; \underline{\mathbf{x}}) &= \lambda \mathcal{L}_{\mathcal{Q}_q}(\beta_{\mathcal{Q}_q}, f_{\mathbf{W}}^{\frac{1}{d}}; \underline{\mathbf{x}}) + \\ &\quad (1 - \lambda) [\mathcal{L}_{\mathcal{G}}(\beta_{\mathcal{G}}, f_{\mathbf{W}}^{\frac{1}{d}}; \beta_{\mathcal{Q}_q} f_{\mathbf{W}}^{\frac{1}{d}}, \underline{\mathbf{x}}) + \mathcal{L}_{\mathcal{W}}(f_{\mathbf{W}}; \mathcal{E}, \underline{\mathbf{x}})] \end{aligned} \quad (16)$$

with respect to $\beta_{\mathcal{Q}_q}$, $\beta_{\mathcal{G}}$, and $f_{\mathbf{W}}$, and where $\lambda \in (0, 1)$ is a mixing hyperparameter.

In combining the shape of \mathcal{Q}_q with those of \mathcal{G} and \mathcal{W} , the number of exceedances of the estimated \mathcal{Q}_q may change at each gradient descent step. Letting $\mathcal{L}_{\mathcal{G}}$ and $\mathcal{L}_{\mathcal{W}}$ be mean negative log-likelihoods instead of negative log-likelihoods ensures that the sum in $\mathcal{L}_{\mathcal{Q}_q, \mathcal{G}, \mathcal{W}}$ is not minimised by minimising the number of exceedances. This same argument is applied to M_2 and M_4 to M_7 in which the shape of \mathcal{G} is also tied to those of \mathcal{Q}_q or \mathcal{W} .

Models M_2 – M_3 : The procedure to fit models M_2 and M_3 borrows from that of M_0 and M_1 in that a pair of their parameters is inferred jointly while the third is estimated independently. Figure 2 indicates, via solid edges, the losses among $\mathcal{L}_{\mathcal{Q}_q}$, $\mathcal{L}_{\mathcal{G}}$, and $\mathcal{L}_{\mathcal{W}}$ that must be combined into a joint loss. Obtaining estimates $\hat{\mathcal{Q}}_q$ and $\hat{\mathcal{G}}$ for M_2 first involves minimising

$$\mathcal{L}_{\mathcal{Q}_q, \mathcal{G}}(\beta_{\mathcal{Q}_q}, \beta_{\mathcal{G}}, f_{\mathcal{G}}; \underline{\mathbf{x}}) = \lambda \mathcal{L}_{\mathcal{Q}_q}(\beta_{\mathcal{Q}_q}, f_{\mathcal{G}}; \underline{\mathbf{x}}) + (1 - \lambda) \mathcal{L}_{\mathcal{G}}(\beta_{\mathcal{G}}, f_{\mathcal{G}}; \beta_{\mathcal{Q}_q} f_{\mathcal{G}}, \underline{\mathbf{x}}), \quad (17)$$

and then $\mathcal{L}_{\mathcal{W}}$ in (15) to infer $\hat{\mathcal{W}}$. Similarly, model M_3 can be fitted by first obtaining an estimate $\hat{\mathcal{Q}}_q$ via the minimisation of $\mathcal{L}_{\mathcal{Q}_q}$ in (13), and then $\hat{\mathcal{G}}$ and $\hat{\mathcal{W}}$ by minimising

$$\mathcal{L}_{\mathcal{G}, \mathcal{W}}(\beta_{\mathcal{G}}, f_{\mathbf{W}}; r_{\hat{\mathcal{Q}}_q}, \underline{\mathbf{x}}) = \mathcal{L}_{\mathcal{G}}(\beta_{\mathcal{G}}, f_{\mathbf{W}}^{1/d}; r_{\hat{\mathcal{Q}}_q}, \underline{\mathbf{x}}) + \mathcal{L}_{\mathcal{W}}(f_{\mathbf{W}}; \mathcal{E}, \underline{\mathbf{x}}). \quad (18)$$

Models M₄–M₇: Models M₄ to M₇ require a different treatment as they involve an additional normalising flow $h_{\mathcal{D}}$ associated with a deformation set \mathcal{D} . The appropriate loss for each of these combines the individual losses $\mathcal{L}_{\mathcal{Q}_q}$, $\mathcal{L}_{\mathcal{G}}$, and $\mathcal{L}_{\mathcal{W}}$ according to the solid or dashed edges depicted in Figure 2. That is, model M₄ shares the same composite loss as M₂, M₅ the same as M₃, and M₆ and M₇ the same as M₁, with the exception that their arguments $r_{\mathcal{Q}_q}$ and $r_{\mathcal{G}}$ are replaced by the appropriate radial functions given in Table 1 and that a penalisation term for the deformation set \mathcal{D} is added. The penalisation term $\lambda_U \overline{\text{D}}_{\text{KL}}[f_U \| f_{\mathcal{D}}]$ —made explicit in Section S.4, with $\lambda_U \geq 0$ controlling the strength of penalisation—is a weighted Monte Carlo approximation of the Kullback–Leibler (KL) divergence of the uniform density f_U on \mathbb{S}^{d-1} from $f_{\mathcal{D}}$; it ensures that $f_{\mathcal{D}}$ is penalised for departure from f_U . This is akin to a penalised complexity prior (Simpson et al., 2017) that puts an exponential prior on the KL divergence to shrink complex models toward a simpler counterpart. The models are fitted by alternately minimising, at every gradient descent iteration, the appropriate loss with respect to $f_{\mathcal{D}}$ (conditionally on the other model parameters) and to the other model parameters (conditionally on $f_{\mathcal{D}}$).

Fitting the above models requires fixing the hyperparameter λ and the penalisation constant λ_U , both determining which composite loss components bear more weight. To avoid significant computational overhead, in the following sections we select a λ which empirically leads to roughly equal contributions of $\lambda \mathcal{L}_{\mathcal{Q}_q}$ and $(1 - \lambda)(\mathcal{L}_{\mathcal{G}} + \mathcal{L}_{\mathcal{W}})$ to the loss $\mathcal{L}_{\mathcal{Q}_q, \mathcal{G}, \mathcal{W}}$ (16) of model M₁, and of $\lambda \mathcal{L}_{\mathcal{Q}_q}$ and $(1 - \lambda)\mathcal{L}_{\mathcal{G}}$ to the loss $\mathcal{L}_{\mathcal{Q}_q, \mathcal{G}}$ (17) of model M₂. In both cases, however, classical selection methods such as cross-validation may be used.

In practice, we minimise the above losses via gradient descent using the *PyTorch* implementation of the *Adam* optimiser (Kingma and Ba, 2017).

3.4 Model regularisation

Due to the possibility of model overfitting, we discuss regularisation techniques that can be applied to our proposed statistical inference methodology.

A first way to reduce overfitting consists in performing early stopping (Prechelt, 2012). Defining training and validation sets $\underline{\mathbf{x}}_T$ and $\underline{\mathbf{x}}_V$ by partitioning the observed data $\underline{\mathbf{x}}$, early stopping involves halting the gradient descent procedure on a loss evaluated at $\underline{\mathbf{x}}_T$ when the loss at $\underline{\mathbf{x}}_V$ has not decreased in a certain number of iterations. This prevents a decrease of the training loss at the detriment of increasing the generalisation error.

A second type of model regularisation technique, called data mollification, has been proposed by Song et al. (2021), and Tran et al. (2023) provided evidence of great improvement to density estimation and to the quality of generated samples in likelihood-based generative models such as normalising flows. Mollification consists in adding gradually-vanishing noise to the data at training time to create a transition from a noisier and simple-to-optimize density to the target density of the data. To avoid deforming the tail properties of the variable $R \mid \mathbf{W}$, we only mollify the training directions $\{\mathbf{x}/\|\mathbf{x}\| : \mathbf{x} \in \underline{\mathbf{x}}_T\}$ by adding independent von Mises noise with gradually-decreasing dispersion parameter σ . Concretely, at the j th of J gradient descent iterations of the training period, we use the mollified dataset

$$\underline{\mathbf{x}}_{T,j} = \{\|\mathbf{x}_i\|\mathbf{w}_{i,\varepsilon} : \mathbf{w}_{i,\varepsilon} \sim \text{vonMises}(\mathbf{x}_i/\|\mathbf{x}_i\|, \sigma_j), \mathbf{x}_i \in \underline{\mathbf{x}}_T\}, \quad (19)$$

where $\text{vonMises}(\boldsymbol{\mu}, \sigma)$ denotes the von Mises distribution with location $\boldsymbol{\mu} \in \mathbb{S}^{d-1}$ and dispersion $\sigma \in \mathbb{R}_{>0}$. Following the logistic decay proposed by Tran et al. (2023), we impose that σ_j decreases to 0 as j increases to J , see Section S.5 for details.

Combining both regularisation methods yields a sensible procedure which stops the

training when the gradient descent algorithm starts overfitting the (decreasingly mollified) data $\underline{\mathbf{x}}_{\text{T},j}$ and increases the generalisation error on the validation data $\underline{\mathbf{x}}_{\text{V}}$.

3.5 Rare event probability estimation

In this section, we detail a method to extrapolate beyond the range of observed data $\underline{\mathbf{x}} = \{\mathbf{x}_1, \dots, \mathbf{x}_n\}$ —assumed to form a random sample from $\mathbb{P}_{\mathbf{X}}$ —and to estimate the probability $\mathbb{P}[\mathbf{X} \in \mathcal{R}]$ that a new draw \mathbf{X} lies in a Borel risk region $\mathcal{R} \subset \mathbb{R}^d$.

Given estimates $\hat{\mathcal{Q}}_q$, $\hat{\mathcal{G}}$, and $\hat{\mathcal{W}}$, and following the procedure outlined in Papastathopoulos et al. (2025), we partition \mathcal{R} into two disjoint regions $\mathcal{R} \cap \hat{\mathcal{Q}}'_q$ and $\mathcal{R} \cap \hat{\mathcal{Q}}_q$ to write

$$\mathbb{P}[\mathbf{X} \in \mathcal{R}] = \mathbb{P}[\mathbf{X} \in \mathcal{R} \mid \mathbf{X} \notin \hat{\mathcal{Q}}_q] \mathbb{P}[\mathbf{X} \notin \hat{\mathcal{Q}}_q] + \mathbb{P}[\mathbf{X} \in \mathcal{R} \cap \hat{\mathcal{Q}}_q]. \quad (20)$$

By model assumptions, $\mathcal{R} \cap \hat{\mathcal{Q}}'_q$ is a region over which our threshold exceedance model is defined; the method described below is especially suited for risk regions \mathcal{R} such that $\mathcal{R} \cap \hat{\mathcal{Q}}_q$ is minimal or null. Assuming that excesses above $\hat{\mathcal{Q}}_q$ follow a multivariate radial exponential distribution with scale $\hat{\mathcal{G}}$ and directions $\hat{\mathcal{W}}$ exactly, we estimate $\mathbb{P}[\mathbf{X} \in \mathcal{R} \mid \mathbf{X} \notin \hat{\mathcal{Q}}_q]$ of equation (20) via a Monte Carlo approximation of the outer integral in (5), *i.e.*,

$$\frac{1}{m} \sum_{i=1}^m \int_{\rho([\mathbf{0}:\mathbf{w}_i^*] \cap \mathcal{R} \cap \hat{\mathcal{Q}}'_q)} \frac{1}{r_{\hat{\mathcal{G}}}(\mathbf{w}_i^*)} \exp \left\{ -\frac{r - r_{\hat{\mathcal{Q}}_q}(\mathbf{w}_i^*)}{r_{\hat{\mathcal{G}}}(\mathbf{w}_i^*)} \right\} dr, \quad (21)$$

where directions $\mathbf{w}_1^*, \dots, \mathbf{w}_m^* \in \mathbb{S}^{d-1} \setminus S_d$ are sampled from $\hat{f}_{\mathbf{W}}$. Notably, the integral in expression (21) is solved exactly whenever the set $\rho([\mathbf{0}:\mathbf{w}] \cap \mathcal{R} \cap \hat{\mathcal{Q}}'_q)$ is known. In the important case where \mathcal{R} is a hyperbox, $\rho([\mathbf{0}:\mathbf{w}] \cap \mathcal{R} \cap \hat{\mathcal{Q}}'_q)$ is a single interval with explicit lower- and upper-bounds (see Section S.6). A simple adaptation yields a method to estimate the probability that at least $j \in \{1, \dots, d\}$ of the components of \mathbf{X} fall below

or above some specified lower- and upper-bounds (see Section S.7).

To estimate the probabilities $\mathbb{P}[\mathbf{X} \notin \hat{\mathcal{Q}}_q]$ and $\mathbb{P}[\mathbf{X} \in \mathcal{R} \cap \hat{\mathcal{Q}}_q]$ of equation (20), we use their respective unbiased empirical estimates

$$\frac{1}{n} \sum_{i=1}^n \mathbb{1}[\mathbf{x}_i \notin \hat{\mathcal{Q}}_q] \quad \text{and} \quad \frac{1}{n} \sum_{i=1}^n \mathbb{1}[\mathbf{x}_i \in \mathcal{R} \cap \hat{\mathcal{Q}}_q]. \quad (22)$$

Their combination with estimate (21) via equation (20) yields an estimate of $\mathbb{P}[\mathbf{X} \in \mathcal{R}]$.

In practice, the sample of directions $\mathbf{w}_1^*, \dots, \mathbf{w}_m^*$ required to evaluate expression (21) is obtained efficiently via the generative property of the normalising flow even for large m , and the calculation of the estimates (22) requires a single iteration through $\underline{\mathbf{x}}$.

4 Simulation study

In this section, we apply the methodology described in Section 3 to demonstrate the ability of our models from Section 2 to accurately estimate the probability of extreme events.

For each $d \in \{3, 5, 7, 10\}$, we draw independent samples from the d -dimensional multivariate normal distribution with zero mean and a randomly generated covariance matrix, resulting in four different simulation study settings. We transform the standard normal marginal distributions to the standard Laplace distribution via the probability integral and inverse transforms—using the exact standard normal and inverse standard Laplace CDFs—to assess the performance of the joint model only, as the marginal model proposed in Section 3.1 is standard and widely adopted.

For each setting, we define three risk regions, $\mathcal{R}_1, \mathcal{R}_2, \mathcal{R}_3 \in \mathbb{R}^d$, for which we can reliably calculate the true probability that a draw from the specified multivariate distributions lies in. In all four settings, \mathcal{R}_1 corresponds to a risk region where all variables are simultane-

ously large; \mathcal{R}_2 and \mathcal{R}_3 are arbitrary hyperbox extremal regions, some corresponding to marginalisation over a subset of the d -dimensional vector. These hyperboxes are explicitly stated in the relevant result figures. For brevity, we only present results from models M_0 , M_1 , and M_2 , since model M_3 was already studied by Papastathopoulos et al. (2025). More results on M_4 to M_7 and visualisations of deformation sets are found in Section S.8.

To highlight the wide applicability and flexibility of our modelling framework, we use the same normalising flow architecture in all four settings—namely, of 5 stacked rational-quadratic spline flows with six knots on each interval of the hypercylinder, see Section S.2. More complex architectures were tested in the same settings and yielded very similar results. To make our probability estimation procedure robust against overfitting, we rely both on early stopping, with a 0.7–0.3 proportion split for the training and validation sets, and on mollification (recall Section 3.4). Further, to ensure roughly equal weights of loss components (see Section 3.3), we fix the mixing hyperparameter λ to 0.8.

For dimensions $d \in \{3, 5, 7\}$, we draw 100 independent samples of size $n = 10^4$ and set the quantile set level to $q = 0.9$ in all settings to assess the effect of the dimension d on the model fitting and probability estimation procedures. We fit models M_0 , M_1 , and M_2 to each sample from each setting as well as to 250 bootstrapped samples from each original sample, allowing us to perform probability estimation and build 95% equal-tailed confidence intervals for the probability of hitting the risk regions \mathcal{R}_1 , \mathcal{R}_2 , and \mathcal{R}_3 . Figure 4 displays boxplots of the base-10 logarithm of 100 probability estimates and of lower- and upper-bounds of the 95% equal-tailed bootstrap confidence intervals. The results illustrate the bias–variance trade-off entailed by the parsimony–flexibility range of models M_0 , M_1 , and those that bridge them. Indeed, it is apparent from Figure 4 that M_0 has less bias than M_1 and that M_1 has narrower confidence intervals than M_0 ; M_2 appears to be a sen-

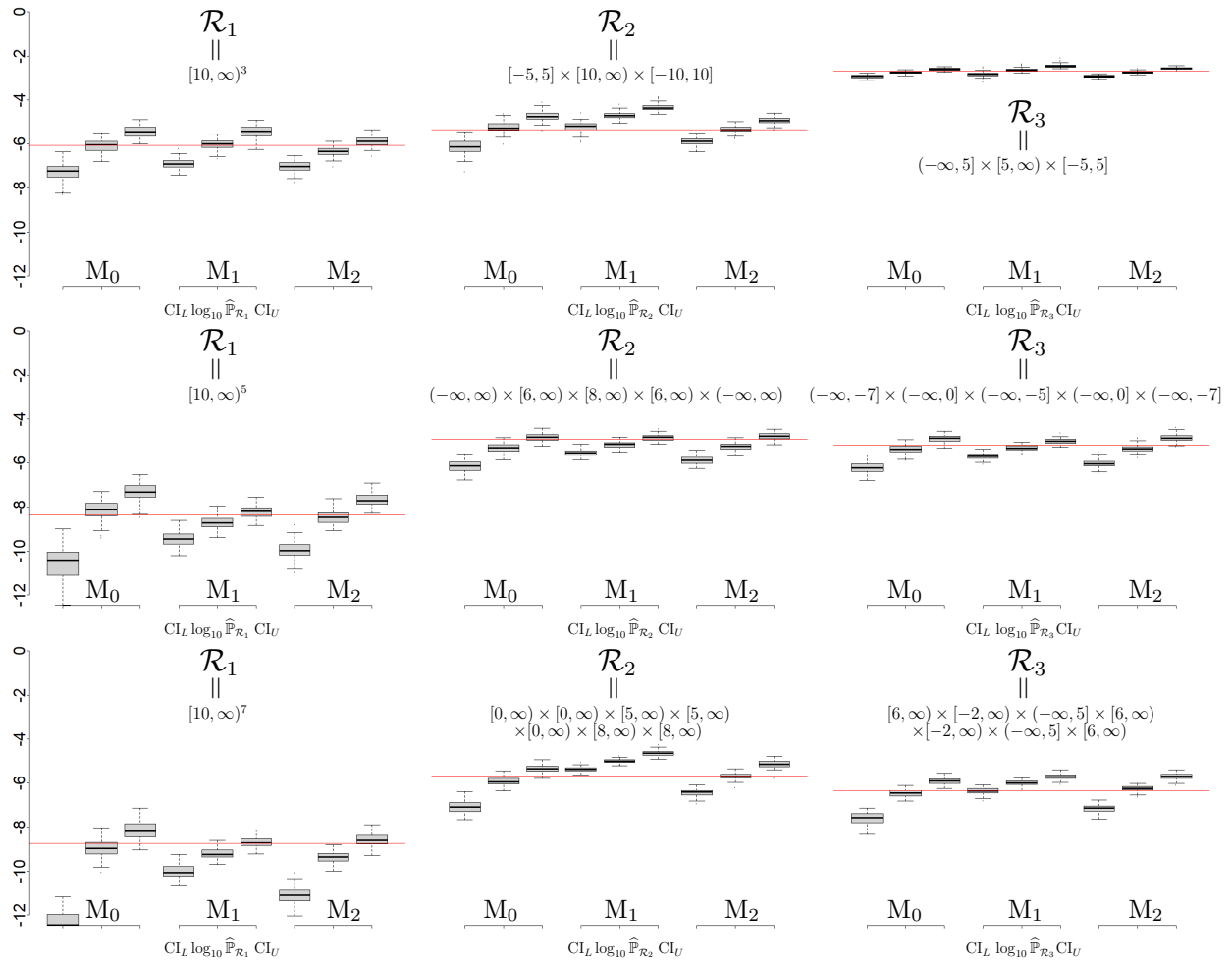


Figure 4: Boxplots of 100 estimated probabilities $\hat{\mathbb{P}}_{\mathcal{R}_j}$, $j = 1, 2, 3$, and of the lower- (CI_L) and upper-bounds (CI_U) of their 95% bootstrap confidence intervals (on \log_{10} scale) for the sets $\mathcal{R}_1, \mathcal{R}_2, \mathcal{R}_3$ using models M_0, M_1 , and M_2 fitted on samples of size $n = 10^4$ from multivariate normal distributions with $d = 3$ (top row), $d = 5$ (middle row), and $d = 7$ (bottom row). The true \log_{10} -probabilities are denoted by red lines.

sible compromise with accurate probability estimates. Further, as expected, the bootstrap confidence intervals for the probability estimates widen with increasing d , reflecting the sparsification of data entailed by increasing dimension.

Figure 12 in Section S.8 of the Supplementary material displays the results of the same experiments for model M_2 with $d \in \{3, 5, 7\}$, and alternative sample sizes of $n = 5000$, 20000, and 20000, as well as probability levels $q = 0.8, 0.95, 0.95$. It illustrates that the method works well in lower dimensions on an extrapolation task corresponding to events way beyond the range of observed data, especially for \mathcal{R}_1 .

Last, we apply our methodology to $d = 10$ dimensions. Figure 13 of Section S.8 shows the results using samples sizes $n = 5 \times 10^4$, 10^5 , and 2×10^5 and probability levels $q = 0.9$, 0.95 , and 0.9625 . While results are not as accurate as in lower dimensions, they are still very decent given the difficulty of the estimation task. Furthermore, we observe that the bias decreases when increasing n and q .

5 Data application to low and high wind extremes

5.1 Data and scientific problem

We apply our methodology to model low and high wind speed data and estimate the probability of multivariate extreme events that may have significant impact on electricity production. The method allows modelling the extremal dependence of events at distinct sites in an unstructured manner. We show that our method can be used to select new sites at which to build wind farms—to minimise or maximise electricity production risk functionals—or to guide management of operations at existing stations especially when terrain or landmarks weaken the belief in spatial modelling assumptions.

The wind speeds are recorded hourly in meters per second (m/s) between 9:00 AM on January 1, 2012, and 8:00 AM on January 1, 2015, at 20 stations near the Oregon and Washington states' border. Figure 5 displays the station locations over the region of the Pacific Northwest, United States (US), which has large wind energy resources (Hering and Genton, 2010; Kazor and Hering, 2015). The data were analysed by Huser et al. (2017) and Castro-Camilo et al. (2019), adopting spatial approaches to model extremal dependence.

We consider the GE 1.5 megawatt (MW) wind turbine—a baseline in the study of wind speed forecasting by Hering and Genton (2010) over the same region—to define low and

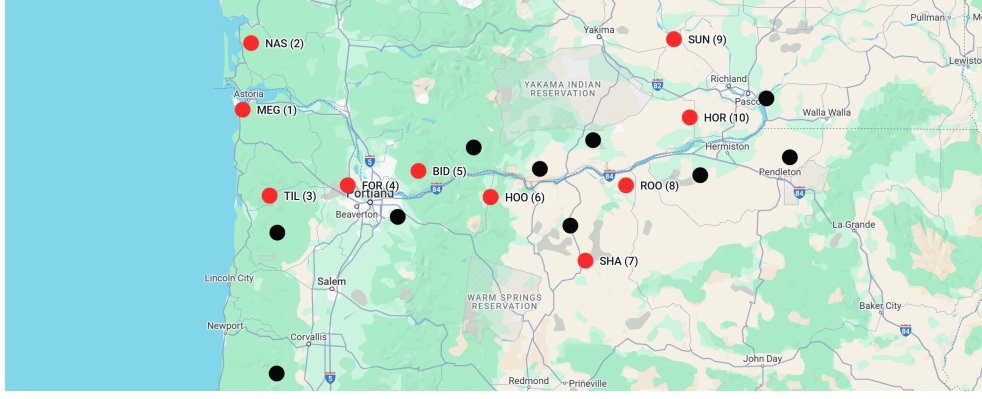


Figure 5: Stations (dots) over the Pacific Northwest region, US, between the Oregon and Washington states. Sites without missing data are in red, numbered from west to east.

high extremes of wind speeds. According to the GE 1.5 MW power curve, wind speeds (m/s) can be partitioned into four intervals $I_1 = [0, 3.5)$, $I_2 = [3.5, 13.5)$, $I_3 = [13.5, 25)$, and $I_4 = [25, \infty)$, with I_1 and I_4 corresponding to too low and too high wind speeds leading to no electricity production and I_3 corresponding to maximal power being produced.

5.2 Data preprocessing

To avoid missingness complications—whose treatment lies outside the scope of this exposition—we consider the 10 stations at which there are no missing observations over the whole time period. These are coloured red and numbered from west to east in Figure 5; their acronyms are detailed in Table 3 of Section S.9. We denote by $\underline{\mathbf{x}}^o = \{\mathbf{x}_i^o = (x_{i,1}^o, \dots, x_{i,10}^o) \in \mathbb{R}_{\geq 0}^{10} : i = 1, \dots, n\}$ the collection assumed to have been observed from the climatology random vector $\mathbf{X}^o \in \mathbb{R}^{10}$.

The data display seasonality patterns which can be observed on monthly and hourly scales, see Figure 6. We adopt a site-wise modelling of wind speeds using the generalised additive model (GAM; Wood, 2011) framework. Following classical approaches (Elliott et al., 2004), we model the site-wise wind speed random variable $X_{j,m,h}^o$, at station j in month m of the year and hour h of the day, under the working assumption that it follows

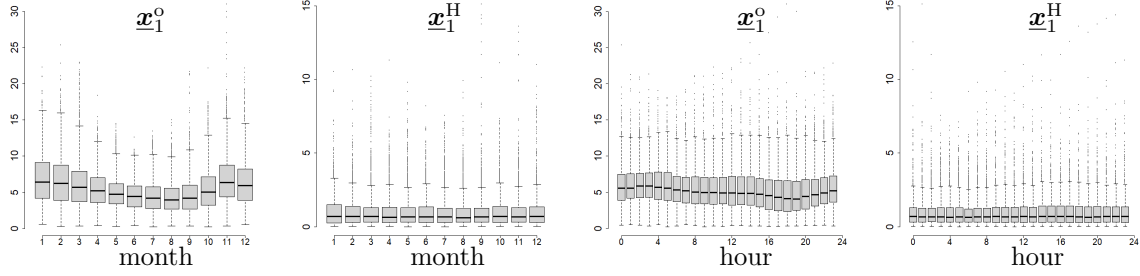


Figure 6: Boxplots of the monthly- and hourly-aggregated original wind speeds (m/s) \underline{x}_1^o (pannels 1-3) and of the homogenised data \underline{x}_1^H (pannels 2-4), respectively, for site MEG.

a Weibull distribution with scale $\lambda_{j,m,h} > 0$ and shape $\kappa_{j,m,h} > 0$. More precisely,

$$X_{j,m,h}^o \sim \text{Weibull}(\lambda_{j,m,h} = s_{j,1}(m) + s_{j,2}(h), \kappa_{j,m,h} = s_{j,3}(m) + s_{j,4}(h)), \quad (23)$$

where s denotes a cubic cyclic spline on $m \in \{1, \dots, 12\}$ or $h \in \{0, \dots, 23\}$.

We fit model (23) using the `evgam` package (Youngman, 2022) from the **R** programming language and obtain estimates $\hat{\lambda}_{j,m,h}$ and $\hat{\kappa}_{j,m,h}$ for all months m and hours h . We obtain homogenised data $\underline{x}^H = \{\underline{x}_i^H = (x_{i,1}^H, \dots, x_{i,10}^H) : i = 1, \dots, n\}$ via $x_{i,j}^H := (x_{i,j}^o / \hat{\lambda}_{j,m,h})^{\hat{\kappa}_{j,m,h}}$ for the month m and hour h of \underline{x}_i . Figure 6 shows monthly- and hourly-aggregated boxplots of the homogenised \underline{x}_1^H at site MEG, where $\underline{x}_j^H := \{x_{i,j}^H : i = 1, \dots, n\}$, being much more homogeneous in time than their original-scale counterparts. Autocorrelation function plots in Figure 14 of Section S.9 also support this: the \underline{x}^H remain autocorrelated for up to approximately four days, considerably less than \underline{x}^o .

Since wind speeds may not follow a Weibull distribution exactly—with misspecification particularly pronounced in the lower and upper tails (Gunturu and Schlosser, 2012)—we apply the marginal model detailed in Section 3.1 to the homogenised observations \underline{x}^H . Due to the known marginal lower-bound of 0 m/s windspeeds, we only model the upper-tails and set the threshold $u_{j,+}$ to the 0.995 empirical quantile of \underline{x}_j^H , respectively, for $j = 1, \dots, 10$. Figure 15 in Section S.9 displays Quantile-Quantile plots of all upper-tail

fits, which suggest that the marginal fits are all satisfactory. We thus obtain $\underline{\mathbf{x}} := \{\mathbf{x}_i := (\hat{\varphi}_1(x_{i,1}^H), \dots, \hat{\varphi}_d(x_{i,d}^H)) : i = 1, \dots, n\}$.

5.3 Geometric extremes modelling

A first event of interest is the event $E_{m,h}^{(1,\mathcal{I})} := \{X_{j,m,h}^o \in I_1 \cup I_4, \forall j \in \mathcal{I}\}$ that a configuration of $\#\mathcal{I}$ stations denoted by the index set $\mathcal{I} \subseteq \{1, \dots, d\}$ does not produce any electricity at hour h of a given day of month m . A second event of interest is that all $\#\mathcal{I}$ stations in configuration \mathcal{I} produce maximal power, that is, $E_{m,h}^{(2,\mathcal{I})} := \{X_{j,m,h}^o \in I_3, \forall j \in \mathcal{I}\}$. Both events can be interpreted in relation to hyperboxes for which the radial integration bounds of equation (5) can respectively be obtained from Sections S.7 and S.6.

To estimate the probability of these events, we transform the hyperboxes from the original scale of the data $\underline{\mathbf{x}}^o$ to the approximate standard Laplace scale of the data $\underline{\mathbf{x}}$. For a general hyperbox $\mathcal{R} := [\mathcal{R}_{1,l}, \mathcal{R}_{1,u}] \times \dots \times [\mathcal{R}_{d,l}, \mathcal{R}_{d,u}]$, we obtain the associated hyperbox $\mathcal{R}_L^{m,h}$ for month m and hour h in the approximate standard Laplace scale via

$$\mathcal{R}_L^{m,h} = \prod_{j=1}^d \left[\hat{\varphi}_j \left(\left(\mathcal{R}_{j,l} / \hat{\lambda}_{j,m,h} \right)^{\hat{\kappa}_{j,m,h}} \right), \hat{\varphi}_j \left(\left(\mathcal{R}_{j,u} / \hat{\lambda}_{j,m,h} \right)^{\hat{\kappa}_{j,m,h}} \right) \right]. \quad (24)$$

We focus on model M₂ and use the same normalising flow architecture as that described in Section 4, having demonstrated its applicability to the range of dimensions studied. We set the probability level of \mathcal{Q}_q to $q = 0.95$, and similarly to the simulation study, we rely on mollification and early stopping, partitioning $\underline{\mathbf{x}}$ into the training and validation sets $\underline{\mathbf{x}}_T$ and $\underline{\mathbf{x}}_V$ according to a 0.7–0.3 proportion split. Due to the temporal autocorrelation in $\underline{\mathbf{x}}^H$ (see Section 5.2), and thus in $\underline{\mathbf{x}}$, we build confidence intervals for our probability estimates via temporal block bootstrapping. We form blocks of 7×24 hours to retain sequences of 7 days of observations which are representative of the temporal dependence in $\underline{\mathbf{x}}$, and fit

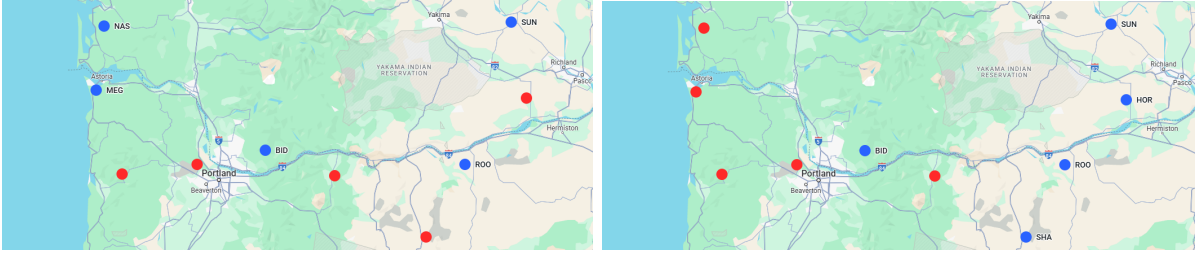


Figure 7: Configurations of five stations (blue) minimising the risk of no production (left) and maximising the probability of full production (right) for month $m = 1$ and hour $h = 18$.

Table 2: Probability estimates and 95% block bootstrap confidence intervals of the three configuration of five stations minimising the probability of no production and maximising that of full production for month $m = 1$ and hour $h = 18$.

Event	Rank	$\hat{\mathbb{P}}_{\mathbf{X}_J}(E_{1,18}^{(e,\mathcal{I})})$	$\text{CI}_{0.95}$	Stations \mathcal{I}
No production ($E_{1,18}^{(1,\mathcal{I})}$)	1	0.0298	[0.0233, 0.0354]	BID, MEG, NAS, ROO, SUN
	2	0.0313	[0.0254, 0.0370]	BID, NAS, ROO, SHA, SUN
	3	0.0332	[0.0283, 0.0376]	BID, HOO, NAS, ROO, SUN
Full production ($E_{1,18}^{(2,\mathcal{I})}$)	1	1.82×10^{-4}	$[4.64 \times 10^{-5}, 3.73 \times 10^{-4}]$	BID, HOR, ROO, SHA, SUN
	2	1.14×10^{-4}	$[3.99 \times 10^{-5}, 2.41 \times 10^{-4}]$	HOR, MEG, ROO, SHA, SUN
	3	1.04×10^{-4}	$[1.95 \times 10^{-5}, 3.57 \times 10^{-4}]$	MEG, NAS, SHA, SUN, TIL

model M_2 to all $\binom{10}{5} = 252$ configurations of $\#\mathcal{I} = 5$ stations. Figure 16 of Section S.9 displays goodness-of-fit plots for a subset of configurations.

Figure 7 and Table 2 show, for the winter month of January ($m = 1$) at a high electricity consumption time of 6:00 PM ($h = 18$), the configurations of five stations minimising the probability of producing no electricity and those maximising the probability of full electricity production. In particular, this latter configuration contains four of the five stations located at the highest altitudes where there are less terrain obstacles and stronger winds. Figure 17 of Section S.9 shows, for the same month m and hour h , the configuration with the highest estimated probability 0.273 of suffering no electricity production, illustrating the important risk gap among different configurations. The west-east alignment of stations in this configuration reflects the correlation identified by Huser et al. (2017) between

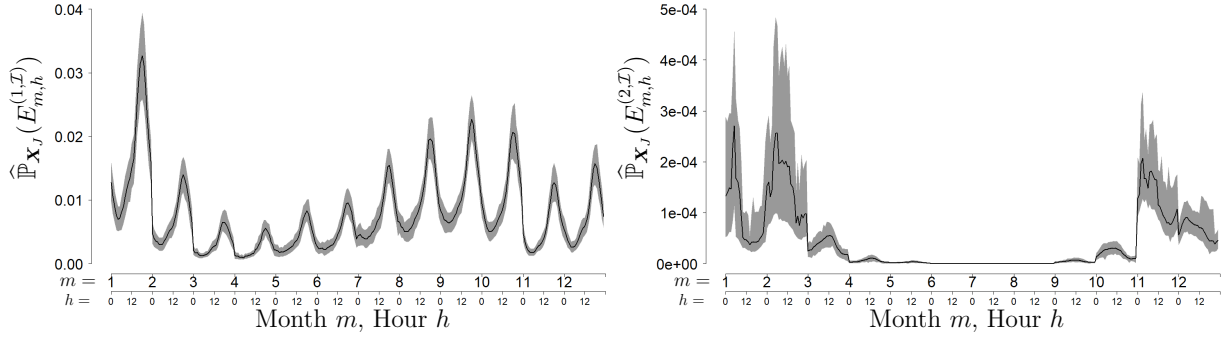


Figure 8: Estimated probability (solid line) and 95% block bootstrap confidence intervals (shaded band) of the event $E_{m,h}^{(1,\mathcal{I})}$ of no power production (left) and of the event $E_{m,h}^{(2,\mathcal{I})}$ of full power production (right) as a function of the month m and the hour h at observation stations $\mathcal{I} = \{\text{BID, MEG, NAS, ROO, SUN}\}$.

stations aligned in the direction of dominant winds.

For the configuration $\mathcal{I} = \{\text{BID, MEG, NAS, ROO, SUN}\}$ of stations which minimises $\hat{\mathbb{P}}_{\mathbf{X}_J}(E_{1,18}^{(1,\mathcal{I})})$, we estimate $\{\mathbb{P}_{\mathbf{X}_J}(E_{m,h}^{(e,\mathcal{I})}) : m = 1, \dots, 12; h = 0, \dots, 23; e = 1, 2\}$, the probabilities of observing no or full electricity production for each month m and hour h . Estimates and their associated 95% block bootstrap confidence intervals are presented in Figure 8. The results display clear periodicity along the different months and times of day the events defined in relation to wind power production. This highlights the potential usefulness of our methods to guide operation management of electricity production.

6 Discussion

Using normalising flows as models for probability densities, we tackled the difficult task of inferring the distribution of directions of multivariate extreme events projected on hyperspheres and built identifiable geometric extremes models by combining the shapes of structural star-body parameters. Leveraging the generative property of normalising flows, we devised a fast and accurate method for the estimation of multivariate extreme events—made even faster via exact integration on radial intervals with explicit bounds whenever

the extreme events of interest can be characterised by hyperboxes. As opposed to classical multivariate extremes frameworks such as those based on the multivariate GP distribution or regular variation, our models can extrapolate in all directions of the multivariate space.

While we adopted the more-parsimonious yet accurate exponential distribution to model the radial exceedances of the quantile set, our methodology could trivially be adapted to use the truncated gamma distribution, akin to Wadsworth and Campbell (2024). Future work could also consider the generalised Pareto model, enforcing regularity on a varying shape function using a penalisation method similar to that used on deformation sets, or the use of normalising flows for conditional density estimation to model non-stationarity.

The code to use our methodology is available at <https://github.com/lambertdem>.

Acknowledgments

Part of this paper was written during a visit of LDM at King Abdullah University of Science and Technology (KAUST). LDM thanks funding from the School of Mathematics, University of Edinburgh (UoE). We acknowledge computing support from the Eddie (UoE) and Ibex (KAUST) high-performance computing clusters.

References

- Balkema, A., P. Embrechts, and N. Nolde (2010). Meta densities and the shape of their sample clouds. *J. Multivar. Anal.* *101*(7), 1738–1754.
- Balkema, G. and N. Nolde (2010). Asymptotic independence for unimodal densities. *Adv. App. Probab.* *42*(2), 411–432.

- Balkema, G. and N. Nolde (2012). Asymptotic dependence for light-tailed homothetic densities. *Adv. App. Probab.* 44(2), 506–527.
- Campbell, R. and J. Wadsworth (2024). Piecewise-linear modeling of multivariate geometric extremes. *arXiv:2412.05195*.
- Castro-Camilo, D., R. Huser, and H. Rue (2019, Sep). A spliced gamma-generalized Pareto model for short-term extreme wind speed probabilistic forecasting. *J. Agric. Biol. Environ. Stat.* 24(3), 517–534.
- Davis, R. A., E. Mulrow, and S. I. Resnick (1988). Almost sure limit sets of random samples in \mathbb{R}^d . *Adv. App. Probab.* 20(3), 573–599.
- Dinh, L., J. Sohl-Dickstein, and S. Bengio (2017). Density estimation using real NVP. In *ICLR*.
- Durkan, C., A. Bekasov, I. Murray, and G. Papamakarios (2019). Neural spline flows. In H. Wallach, H. Larochelle, A. Beygelzimer, F. d'Alché-Buc, E. Fox, and R. Garnett (Eds.), *Adv. Neural Inf. Process. Syst.*, Volume 32. Curran Associates, Inc.
- Elliott, D., M. Schwartz, and G. Scott (2004). Wind resource base. In C. J. Cleveland (Ed.), *Encyclopedia of Energy*, pp. 465–479. New York: Elsevier.
- Fisher, L. (1969). Limiting Sets and Convex Hulls of Samples from Product Measures. *Ann. Math. Stat.* 40(5), 1824 – 1832.
- Geffroy, J. (1958). Contribution à la théorie des valeurs extrêmes. *Ann. ISUP VII*(1), 37–121.
- Geffroy, J. (1959). Contribution à la théorie des valeurs extrêmes (Suite). *Ann. ISUP VIII*(1), 3–65.

- Gunturu, U. B. and C. A. Schlosser (2012). Characterization of wind power resource in the United States. *Atmospheric Chemistry and Physics* 12(20), 9687–9702.
- Hansen, G., I. Herburt, H. Martini, and M. Moszyńska (2020). Starshaped sets. *Aequationes Mathematicae* 94, 1001–1092.
- Hering, A. S. and M. G. Genton (2010). Powering up with space-time wind forecasting. *J. Am. Stat. Assoc.* 105(489), 92–104.
- Hickling, T. and D. Prangle (2023). Flexible tails for normalising flows, with application to the modelling of financial return data. *arXiv:2311.00580*.
- Hu, C. and D. Castro-Camilo (2025). GPDFlow: Generative multivariate threshold exceedance modeling via normalizing flows. *arXiv:2503.11822*.
- Huser, R., T. Opitz, and E. Thibaud (2017). Bridging asymptotic independence and dependence in spatial extremes using Gaussian scale mixtures. *Spatial Statistics* 21, 166–186.
- Kazor, K. and A. S. Hering (2015). The role of regimes in short-term wind speed forecasting at multiple wind farms. *Stat* 4(1), 271–290.
- Kingma, D. P. and J. Ba (2017). Adam: A method for stochastic optimization. *arXiv:1412.6980*.
- Kinoshita, K. and S. I. Resnick (1991). Convergence of scaled random samples in \mathbb{R}^d . *Ann. Probab.* 19(4), 1640–1663.
- Kobyzev, I., S. J. Prince, and M. A. Brubaker (2021). Normalizing flows: an introduction and review of current methods. *IEEE Trans. Pattern Anal. Mach. Intell.* 43(11), 3964–3979.

- Koenker, R. and G. Bassett (1978). Regression quantiles. *Econometrica* 46(1), 33–50.
- Lhaut, S., H. Rootzén, and J. Segers (2025). Wasserstein-Aitchison GAN for angular measures of multivariate extremes. *arXiv:2504.21438*.
- Mackay, E. and P. Jonathan (2024). Modelling multivariate extremes through angular-radial decomposition of the density function. *arXiv:2310.12711*.
- Mackay, E., C. Murphy-Barltrop, J. Richards, and P. Jonathan (2024). Deep learning joint extremes of metocean variables using the SPAR model. *arXiv:2412.15808*.
- Majumder, R., B. A. Shaby, B. J. Reich, and D. S. Cooley (2025). Semiparametric Estimation of the Shape of the Limiting Bivariate Point Cloud. *Bayesian Anal.*, 1 – 27.
- Murphy-Barltrop, C. J. R., E. Mackay, and P. Jonathan (2024). Inference for multivariate extremes via a semi-parametric angular-radial model. *arXiv:2401.07259*.
- Murphy-Barltrop, C. J. R., R. Majumder, and J. Richards (2024). Deep learning of multivariate extremes via a geometric representation. *arXiv:2406.19936*.
- Ng, T. L. J. and A. Zammit-Mangion (2024). Mixture modeling with normalizing flows for spherical density estimation. *Adv. Data Anal. Classif.* 18(1), 103–120.
- Nolde, N. (2014). Geometric interpretation of the residual dependence coefficient. *J. Multivar. Anal.* 123, 85–95.
- Nolde, N. and J. L. Wadsworth (2022). Linking representations for multivariate extremes via a limit set. *Adv. App. Probab.* 54(3), 688–717.
- Papamakarios, G., E. Nalisnick, D. J. Rezende, S. Mohamed, and B. Lakshminarayanan (2021). Normalizing flows for probabilistic modeling and inference. *J. Mach. Learn. Res.* 22(1).

- Papamakarios, G., T. Pavlakou, and I. Murray (2017). Masked autoregressive flow for density estimation. In I. Guyon, U. V. Luxburg, S. Bengio, H. Wallach, R. Fergus, S. Vishwanathan, and R. Garnett (Eds.), *Adv. Neural Inf. Process. Syst.*, Volume 30. Curran Associates, Inc.
- Papastathopoulos, I., L. De Monte, R. Campbell, and H. Rue (2025). Statistical inference for radial generalized pareto distributions and return sets in geometric extremes. *arXiv:2310.06130*.
- Paszke, A., S. Gross, F. Massa, A. Lerer, J. Bradbury, G. Chanan, T. Killeen, Z. Lin, N. Gimelshein, L. Antiga, A. Desmaison, A. Köpf, E. Yang, Z. DeVito, M. Raison, A. Tejani, S. Chilamkurthy, B. Steiner, L. Fang, J. Bai, and S. Chintala (2019). PyTorch: an imperative style, high-performance deep learning library.
- Prechelt, L. (2012). Early stopping — but when? In G. Montavon, G. B. Orr, and K.-R. Müller (Eds.), *Neural Networks: Tricks of the Trade: Second Edition*, Berlin, Heidelberg, pp. 53–67. Springer Berlin Heidelberg.
- Rezende, D. J., G. Papamakarios, S. Racaniere, M. Albergo, G. Kanwar, P. Shanahan, and K. Cranmer (2020). Normalizing Flows on Tori and Spheres. In H. D. III and A. Singh (Eds.), *Proceedings of the 37th International Conference on Machine Learning*, Volume 119 of *Proc. J. Mach. Learn. Res.*, pp. 8083–8092. PMLR.
- Rootzén, H. and N. Tajvidi (2006). Multivariate generalized Pareto distributions. *Bernoulli* 12(5), 917–930.
- Simpson, D., H. Rue, A. Riebler, T. G. Martins, and S. H. Sørbye (2017). Penalising Model Component Complexity: A Principled, Practical Approach to Constructing Priors. *Stat. Sci.* 32(1), 1 – 28.

- Simpson, E. S. and J. A. Tawn (2024a). Estimating the limiting shape of bivariate scaled sample clouds: With additional benefits of self-consistent inference for existing extremal dependence properties. *Electron. J. Stat.* 18(2), 4582 – 4611.
- Simpson, E. S. and J. A. Tawn (2024b). Inference for new environmental contours using extreme value analysis. *J. Agric. Biol. Environ. Stat.*.
- Song, Y., J. Sohl-Dickstein, D. P. Kingma, A. Kumar, S. Ermon, and B. Poole (2021). Score-based generative modeling through stochastic differential equations. In *ICLR*.
- Stimper, V., D. Liu, A. Campbell, V. Berenz, L. Ryll, B. Schölkopf, and J. M. Hernández-Lobato (2023). normflows: a PyTorch package for normalizing flows. *J. Open Source Softw.* 8(86), 5361.
- Tran, B.-H., G. Franzese, P. Michiardi, and M. Filippone (2023). One-line-of-code data mollification improves optimization of likelihood-based generative models. In A. Oh, T. Naumann, A. Globerson, K. Saenko, M. Hardt, and S. Levine (Eds.), *Adv. Neural Inf. Process. Syst.*, Volume 36, pp. 6545–6567. Curran Associates, Inc.
- Wadsworth, J. L. and R. Campbell (2024). Statistical inference for multivariate extremes via a geometric approach. *J. R. Stat. Soc., B* 86(5), 1243–1265.
- Wessel, J. B., C. J. R. Murphy-Barltrop, and E. S. Simpson (2025). A comparison of generative deep learning methods for multivariate angular simulation.
- Wood, S. N. (2011). Fast stable restricted maximum likelihood and marginal likelihood estimation of semiparametric generalized linear models. *J. R. Stat. Soc., B* 73(1), 3–36.
- Youngman, B. D. (2022). evgam: An R package for generalized additive extreme value models. *J. Stat. Softw.* 103(3), 1–26.

SUPPLEMENTARY MATERIAL

S.1 Multivariate radial exponential distribution

The multivariate radial exponential distribution is supported on the complement of a location set $\mathcal{M} \in \star$, and has a scaling set $\Sigma \in \star$ and a directional set $\mathcal{W} \in \star$ with radial function $r_{\mathcal{W}}$ equal to the density of directions $f_{\mathcal{W}}$.

Figure 9 displays a sample from a bivariate radial exponential distribution with scale \mathcal{G} given by $r_{\mathcal{G}}(\mathbf{w}) = \exp\{\sin(5\mathbf{w})/2\}/2$ and directional set \mathcal{W} with $f_{\mathcal{W}} \equiv 1/(2\pi)$, the uniform density on \mathbb{S}^1 . By the memoryless property, $(R - u) \mid \{R > u, \mathbf{W} = \mathbf{w}\} \sim \text{Exp}(1/r_{\mathcal{G}}(\mathbf{w}))$ for any $u > 0$ and $\mathbf{w} \in \mathbb{S}^{d-1}$, and hence, exceedances $\mathbf{X} \mid \{\mathbf{X} \in \mathcal{Q}'_q\}$ follow a radial exponential distribution with location \mathcal{Q}_q and scale \mathcal{G} exactly.

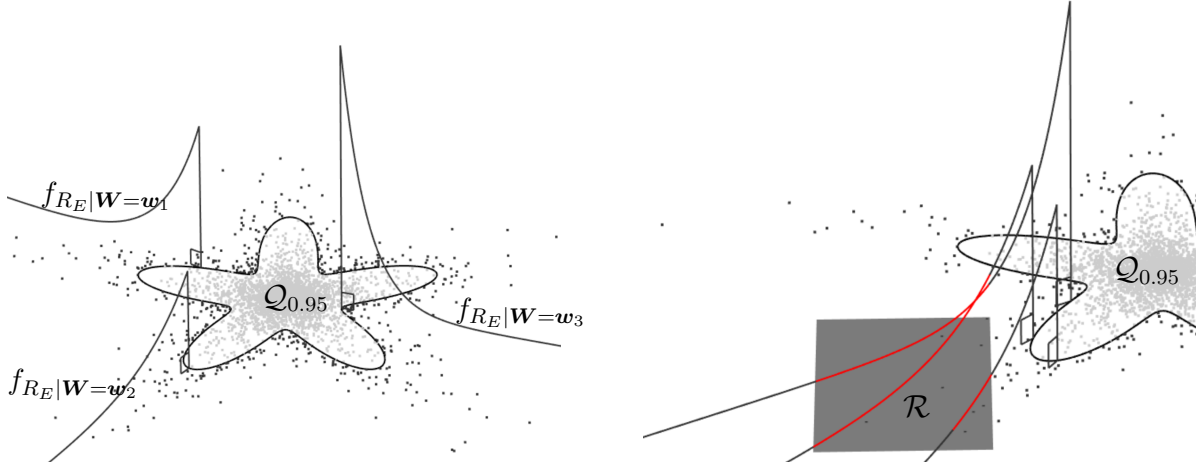


Figure 9: Samples from a bivariate radial exponential distribution with scale \mathcal{G} given by $r_{\mathcal{G}}(\mathbf{w}) = \exp\{\sin(5\mathbf{w})/2\}/2$, associated true quantile set $\mathcal{Q}_{0.95}$, and exceedance samples (dark grey) in the complement $\mathcal{Q}'_{0.95}$. *Left*: Exponential density $f_{R_E|\mathbf{W}=\mathbf{w}}$ of radial exceedances with scale $r_{\mathcal{G}}$ at directions $\mathbf{w}_1, \mathbf{w}_2, \mathbf{w}_3 \in \mathbb{S}^1$. *Right*: Visualisation of expression (5) with integration of the radial density along three directions intersecting with \mathcal{R} .

S.2 Rational-quadratic spline flows formulation

Rezende et al. (2020) proposed to apply a two-stage autoregressive flow to the hypercylinder \mathbb{C}^{d-1} —see their Section 2.3.1 and Appendix B for a detailed description.

The procedure performs transformations based on rational-quadratic splines (Durkan et al., 2019) to the different marginal intervals $[0, 2\pi]$ and $(-1, 1)$ of \mathbb{C}^{d-1} . A transformation g applied to an interval is parameterised by a set of $\Phi + 1$ knots $\{x_\phi, y_\phi\}_{\phi=0}^\Phi$ and Φ slopes $\{s_\phi\}_{\phi=1}^\Phi$ such that $x_{\phi-1} < x_\phi$, $y_{\phi-1} < y_\phi$, and $s_\phi > 0$ for all $\phi = 1, \dots, \Phi$. For $x_{\phi-1} < x < x_\phi$, the transformation g is defined via

$$g(x) = \frac{\alpha_{\phi,2}x^2 + \alpha_{\phi,1}x + \alpha_{\phi,0}}{\beta_{\phi,2}x^2 + \beta_{\phi,1}x + \beta_{\phi,0}}, \quad (1)$$

where the coefficients $\{\alpha_{\phi,i}, \beta_{\phi,i}\}_{i=0}^2$ are constrained so that g is strictly monotonic increasing, $g(x_{\phi-1}) = y_{\phi-1}$, $g(x_\phi) = y_\phi$, and $\partial g(t)/\partial t|_{t=x} = s_\phi$ for all $\phi = 1, \dots, \Phi$. Then, transformations on $(-1, 1)$ are defined by setting $x_0 = y_0 = -1$ and $x_\Phi = y_\Phi = 1$, and circular transformations on $[0, 2\pi]$ by setting $x_0 = y_0 = 0$, $x_\Phi = y_\Phi = 2\pi$, and $s_1 = s_\phi$.

S.3 Transformation from \mathbb{S}^{d-1} to $\mathbb{S}^1 \times (-1, 1)^{d-2}$

Let $T^{(k)}$, for $k \geq 3$, denote the transformation mapping a direction $\mathbf{w} = (w_1, \dots, w_k) \in \mathbb{S}^{k-1}$ to the hypercylinder $\mathbb{S}^{k-2} \times (-1, 1)$ and define it via

$$T^{(k)}(\mathbf{w}) = \left(\frac{\mathbf{w}_{[1:k-1]}}{\sqrt{1 - w_k^2}}, w_k \right), \quad \mathbf{w} \in \mathbb{S}^{k-1} \setminus \left\{ \pm \mathbf{e}_k^{(k)} \right\}, \quad k \geq 3, \quad (2)$$

where $\mathbf{e}_n^{(m)}$ denotes the vector of size n whose sole non-zero m th component is equal to 1.

Defining the transformation $\tilde{T}^{(k)} : \mathbb{S}^{k-1} \times (-1, 1)^{d-k} \rightarrow \mathbb{S}^{k-2} \times (-1, 1)^{d-k+1}$ via

$$\tilde{T}^{(k)}(\mathbf{x}) = \begin{cases} (T^{(k)}(\mathbf{x}_{[1:k]}), \mathbf{x}_{[k+1:d]}), & k < d, \\ T^{(k)}(\mathbf{x}), & k = d, \end{cases} \quad (3)$$

for $\mathbf{x} \in \mathbb{S}^{k-1} \times (-1, 1)^{d-k} \setminus \{\pm \mathbf{e}_d^{(k)}\}$, we have that the recursive and reversible transformation $T := \tilde{T}^{(3)} \circ \dots \circ \tilde{T}^{(d)}$ maps elements of the punctured hypersphere $\mathbb{S}^{d-1} \setminus \{\pm \mathbf{e}_d^{(3)}, \dots, \pm \mathbf{e}_d^{(d)}\}$ into the hypercylinder \mathbb{C}^{d-1} .

Papamakarios et al. (2021) show that the transformation T , for a direction $\mathbf{w} \in \mathbb{S}^{d-1}$ and associated $\mathbf{c} = T(\mathbf{w}) \in \mathbb{C}^{d-1}$, has Jacobian determinant given by

$$\left| \frac{\partial T(\mathbf{w})}{\partial \mathbf{w}} \right| = \prod_{i=1}^d (1 - c_i^2)^{-\left(\frac{i+1}{2}-1\right)}. \quad (4)$$

Numerical instabilities in the computation of the Jacobian determinant can occur whenever c_i is in the near vicinity of -1 or 1 for some $i \in \{1, \dots, d\}$. However, these locations on the hypercylinder correspond to the near vicinity of the singularities S_d of the transformation T expressed in Section 3.2, and hence, have small or negligible measure with respect to $\mathbb{P}_{\mathbf{X}/\|\mathbf{X}\|}$ leading to negligible impact on the general probability estimation procedure.

S.4 Uniform penalisation for constrained models

The PDF of a uniform density on \mathbb{S}^{d-1} is given by $f_U(\mathbf{w}) = \Gamma(d/2)/2\pi^{d/2}$, $\mathbf{w} \in \mathbb{S}^{d-1}$.

Hence, penalisation of $f_{\mathcal{D}}$ away from f_U can be performed via the Kullback–Leibler divergence $D_{\text{KL}}[f_U \| f_{\mathcal{D}}] = \int_{\mathbb{S}^{d-1}} \log[f_U(\mathbf{w})/f_{\mathcal{D}}(\mathbf{w})] f_U(\mathbf{w}) d\mathbf{w}$. In practice, this integral is approximated via Monte Carlo integration by sampling a large number m of directions $\mathbf{u}_1, \dots, \mathbf{u}_m$

uniformly on \mathbb{S}^{d-1} and calculating

$$\overline{\text{D}}_{\text{KL}}[f_U \| f_{\mathcal{D}}] := \frac{1}{m} \sum_{i=1}^m \log[f_U(\mathbf{u}_i)/f_{\mathcal{D}}(\mathbf{u}_i)]. \quad (5)$$

S.5 Mollification dispersion parameter

To perform gradually vanishing mollification, at iteration $j \in \{0, \dots, J\}$, we set

$$\sigma_j = \sigma \frac{\text{Sigmoid}(j/(\tau J)) - \text{Sigmoid}(1/\tau)}{\text{Sigmoid}(0) - \text{Sigmoid}(1/\tau)}, \quad (6)$$

where $\text{Sigmoid}(x) = 1/\{1 + \exp(x)\}$, $\sigma > 0$ is the strength of dispersion at iteration $j = 0$ and $\tau > 0$ controls the rate of decay of σ_j to 0 when $j = J$.

S.6 Radial integration bounds of hyperboxes

Let $\mathbf{a} = (a_1, \dots, a_d) \in \{\mathbb{R} \cup \{-\infty, \infty\}\}^d$ and $\mathbf{b} = (b_1, \dots, b_d) \in \{\mathbb{R} \cup \{-\infty, \infty\}\}^d$, with $a_i \leq b_i$ for all $i \in \{1, \dots, d\}$, then the set $\mathcal{R} = [a_1, b_1] \times \dots \times [a_d, b_d]$ is a hyperbox. Since hyperboxes are starshaped (in the more general sense of Hansen et al. (2020)), for $\mathbf{w} \in \mathbb{S}^{d-1}$, the intersection $[\mathbf{0} : \mathbf{w}) \cap \mathcal{R}$ is either a single line segment—possibly degenerate to a singleton—or empty. For simplicity, we let $\mathcal{S}_{\mathcal{R}} := \{\mathbf{x}/\|\mathbf{x}\| \in \mathbb{S}^{d-1} : \mathbf{x} \in \mathcal{R}\}$ be the set of directions pointing toward \mathcal{R} , so that $[\mathbf{0} : \mathbf{w}) \cap \mathcal{R} = \emptyset$ if and only if $\mathbf{w} \in \mathcal{S}_{\mathcal{R}}$.

We define the functions $r_{\mathcal{R}}^{\text{inf}} : \mathbb{S}^{d-1} \rightarrow \mathbb{R}_{\geq 0}$ and $r_{\mathcal{R}}^{\text{sup}} : \mathbb{S}^{d-1} \rightarrow \mathbb{R}_{\geq 0}$, mapping a direction $\mathbf{w} \in \mathcal{S}_{\mathcal{R}}$ respectively to the infimum and supremum radii of $[\mathbf{0} : \mathbf{w}) \cap \mathcal{R}$ and a direction

$\mathbf{w} \notin \mathcal{S}_{\mathcal{R}}$ to 0, through

$$r_{\mathcal{R}}^*(\mathbf{w}) = \begin{cases} * \{ \|\mathbf{x}\| : \mathbf{x} \in [\mathbf{0} : \mathbf{w}) \cap \mathcal{R} \}, & \mathbf{w} \in \mathcal{S}_{\mathcal{R}}, \\ 0, & \mathbf{w} \notin \mathcal{S}_{\mathcal{R}}, \end{cases} \quad \mathbf{w} \in \mathbb{S}^{d-1}, \quad (7)$$

where $*$ is a place-holder for the inf or sup operators. Knowing $r_{\mathcal{R}}^{\inf}$ and $r_{\mathcal{R}}^{\sup}$ on \mathbb{S}^{d-1} is sufficient to evaluate the inner integral in equation (5), but this requires obtaining an expression for the inf and sup of expressions (7) as well as conditions to determine if a given direction \mathbf{w} belongs to $\mathcal{S}_{\mathcal{R}}$ or not.

We first consider the case in which \mathcal{R} lies entirely in one quadrant of \mathbb{R}^d , that is, for each $i \in \{1, \dots, d\}$, either $a_i \geq 0$ or $b_i \leq 0$. Since $\|\mathbf{x}\|$ is invariant to the sign of $\mathbf{x} \in \mathbb{R}^d$, we map \mathcal{R} to $\mathcal{R}_+ := [a_{1,+}, b_{1,+}] \times \dots \times [a_{d,+}, b_{d,+}]$ where $\mathbf{a}_+ = (\min\{|a_{i,+}|, |b_{i,+}|\} : i = 1, \dots, d)$ and $\mathbf{b}_+ = (\max\{|a_{i,+}|, |b_{i,+}|\} : i = 1, \dots, d)$ in the $\mathbb{R}_{>0}^d$ quadrant, preserving that if $\mathbf{x} \in \mathcal{R}$ maps to $\mathbf{x}_+ \in \mathcal{R}_+$, then $\|\mathbf{x}\| = \|\mathbf{x}_+\|$. Assuming that $\mathbf{w} \in \mathcal{S}_{\mathcal{R}}$, we have that

$$\inf\{\|\mathbf{x}\| : \mathbf{x} \in [\mathbf{0} : \mathbf{w}) \cap \mathcal{R}\} = \max\{\mathbf{a}_+/\mathbf{w}_+\} \quad (8)$$

and

$$\sup\{\|\mathbf{x}\| : \mathbf{x} \in [\mathbf{0} : \mathbf{w}) \cap \mathcal{R}\} = \min\{\mathbf{b}_+/\mathbf{w}_+\}, \quad (9)$$

where $\mathbf{w}_+ = (|w_i| : i = 1, \dots, d)$. The term $\max\{\mathbf{a}_+/\mathbf{w}_+\}$ in (8) is the smallest factor t so that $t\mathbf{w}$ first enters \mathcal{R} . Analogously, the term $\min\{\mathbf{b}_+/\mathbf{w}_+\}$ in (9) is the biggest factor t so that $t\mathbf{w} \in \mathcal{R}$ while $(t + \varepsilon)\mathbf{w} \notin \mathcal{R}$ for all $\varepsilon > 0$.

It remains to determine whether a direction \mathbf{w} belongs to $\mathcal{S}_{\mathcal{R}}$. Again assuming that \mathcal{R} lies entirely in a quadrant of \mathbb{R}^d , we check that $\mathbf{w} \notin \mathcal{S}_{\mathcal{R}}$ if $\min\{\mathbf{a}/\mathbf{w}\} < 0$: if $\min\{\mathbf{a}/\mathbf{w}\} < 0$,

there cannot exist $r > 0$ such that $r\mathbf{w} \in \mathcal{R}$. However, \mathbf{w} could still lie in the same quadrant as \mathcal{R} and lead to $[\mathbf{0} : \mathbf{w}) \cap \mathcal{R} = \emptyset$: we must further verify that $\max\{\mathbf{a}_+/\mathbf{w}_+\} \geq \min\{\mathbf{b}_+/\mathbf{w}_+\}$. If this condition is not met, there does not exist $r > 0$ such that $r\mathbf{w}$ exceeds all components of \mathbf{a} (*i.e.* potentially enters \mathcal{R}) before it exceeds at least one component of \mathbf{b} (*i.e.* potentially exits \mathcal{R}).

The case where \mathcal{R} does not entirely belong to a quadrant of \mathbb{R}^d is dealt with by considering an appropriate subset of \mathcal{R} laying in a single quadrant to apply the same logic as before. Suppose that \mathcal{R} is a hyperbox such that $a_i < 0 < b_i$ for all $i \in J \subseteq \{1, \dots, d\}$, *i.e.* \mathcal{R} lies in more than one quadrant. Then, if $\mathbf{w}_i > 0$ (respectively $\mathbf{w}_i < 0$) and $[\mathbf{0} : \mathbf{w}) \cap \mathcal{R} \neq \emptyset$, then each $\mathbf{x} \in [\mathbf{0} : \mathbf{w}) \cap \mathcal{R}$ must have $x_i > 0$ (respectively $x_i < 0$). Thus, to obtain $r_B^{\text{inf}}(\mathbf{w})$ and $r_B^{\text{sup}}(\mathbf{w})$, it suffices to consider the hyperbox $\mathcal{R}_{\mathbf{w}}$ with lower- and upper-bounds \mathbf{a} and \mathbf{b} such that $a_i = 0$ if $w_i > 0$ or $b_i = 0$ if $w_i < 0$, for each $i \in J$. $\mathcal{R}_{\mathbf{w}}$ then lies entirely in one quadrant of \mathbb{R}^d , and $r_{\mathcal{R}}^{\text{inf}}(\mathbf{w}) = r_{\mathcal{R}_{\mathbf{w}}}^{\text{inf}}(|\mathbf{w}|)$ and $r_{\mathcal{R}}^{\text{sup}}(\mathbf{w}) = r_{\mathcal{R}_{\mathbf{w}}}^{\text{sup}}(|\mathbf{w}|)$ for all $\mathbf{w} \in \mathbb{S}^{d-1}$.

Hence, if \mathcal{R} is a hyperbox and $r_{\mathcal{R}}^{\text{inf}} \geq r_{\mathcal{Q}_q}$, the inner integral in (5) and the integral in (21) simplify according to

$$\mathbb{P}[\mathbf{X} \in \mathcal{R} \mid \mathbf{X} \in \mathcal{Q}'_q, \mathbf{W} = \mathbf{w}] = \int_{r_{\mathcal{R}}^{\text{inf}}(\mathbf{w})}^{r_{\mathcal{R}}^{\text{sup}}(\mathbf{w})} \frac{1}{r_{\mathcal{G}}(\mathbf{w})} \exp\left\{-\frac{r - r_{\mathcal{Q}_q}(\mathbf{w})}{r_{\mathcal{G}}(\mathbf{w})}\right\} dr. \quad (10)$$

S.7 Subset of exceedances

In this section, we derive the radial integration bounds used to compute the probability that at least ℓ of the margins of \mathbf{X} fall below or above their associated negative lower- and positive upper-bounds $\mathbf{l} = (l_1, \dots, l_d) \in \mathbb{R}_{\leq 0}^d$ and $\mathbf{u} = (u_1, \dots, u_d) \in \mathbb{R}_{\geq 0}^d$, respectively, for some $\ell \in \{1, \dots, d\}$. That is, for some index sets A and B such that $A \cup B = \{1, \dots, d\}$ and $A \cap B = \emptyset$, we assume for simplicity that $\mathcal{Q}_q \subseteq \mathcal{H} := [l_1, u_1] \times \dots \times [l_d, u_d]$ and define

$r^{(\ell)} : \mathbb{S}^{d-1} \rightarrow \mathbb{R}_{\geq 0}$ such that

$$\mathbb{P}[\mathbf{X}_A \notin [\mathbf{l}_A, \mathbf{u}_A], \mathbf{X}_B \in [\mathbf{l}_B, \mathbf{u}_B], \#A \geq \ell] = \int_{\mathbf{w} \in \mathbb{S}^{d-1}} \int_{r^{(\ell)}(\mathbf{w})}^{\infty} \frac{1}{r_{\mathcal{G}}(\mathbf{w})} \exp \left\{ -\frac{r - r_{\mathcal{Q}_q}(\mathbf{w})}{r_{\mathcal{G}}(\mathbf{w})} \right\} dr d\mathbf{w}, \quad (11)$$

where $\mathbf{X} \in [\mathbf{x}, \mathbf{y}]$, with $\mathbf{x}, \mathbf{y} \in \mathbb{R}^d$, denotes that $l_i < X_i < u_i$ for all $i \in \{1, \dots, d\}$. The case where $\mathcal{Q}_q \not\subseteq \mathcal{H}$ can be dealt with by resorting to the partitioning method of Section 3.5.

Given a direction $\mathbf{w} \in \mathbb{S}^{d-1}$, the sign of its i th component determines whether $[\mathbf{0} : \mathbf{w})$ points toward the face with coordinate l_i or u_i of the hyperbox \mathcal{H} . Hence, the vector

$$\mathbf{a}(\mathbf{w}, \mathbf{l}, \mathbf{u}) = \left[\max \left\{ \frac{l_1}{w_1}, \frac{u_1}{w_1} \right\}, \dots, \max \left\{ \frac{l_d}{w_d}, \frac{u_d}{w_d} \right\} \right] \quad (12)$$

yields in every ordinate the smallest factor t_i by which \mathbf{w} needs to be multiplied so that $t_i w_i \notin [l_i, u_i]$. Therefore, defining $r^{(\ell)}(\mathbf{w}) = \mathbf{a}(\mathbf{w}, \mathbf{l}, \mathbf{u})_{(\ell)}$ where $\mathbf{x}_{(\ell)}$ denotes the ℓ th smallest component of $\mathbf{x} \in \mathbb{R}^d$, we get that for $r > r^{(\ell)}(\mathbf{w})$, the point $r\mathbf{w} \in \mathbb{R}^d$ has at least ℓ of its coordinates are outside their intervals specified by \mathbf{l} and \mathbf{u} ; that is, some index sets A and B such that $A \cup B = \{1, \dots, d\}$, $A \cap B = \emptyset$, and $\#A \geq \ell$, $r\mathbf{w}_A \notin [\mathbf{l}_A, \mathbf{u}_A]$ and $r\mathbf{w}_B \in [\mathbf{l}_B, \mathbf{u}_B]$. Hence, $r^{(\ell)}$ satisfies equation (11).

S.8 Simulation study

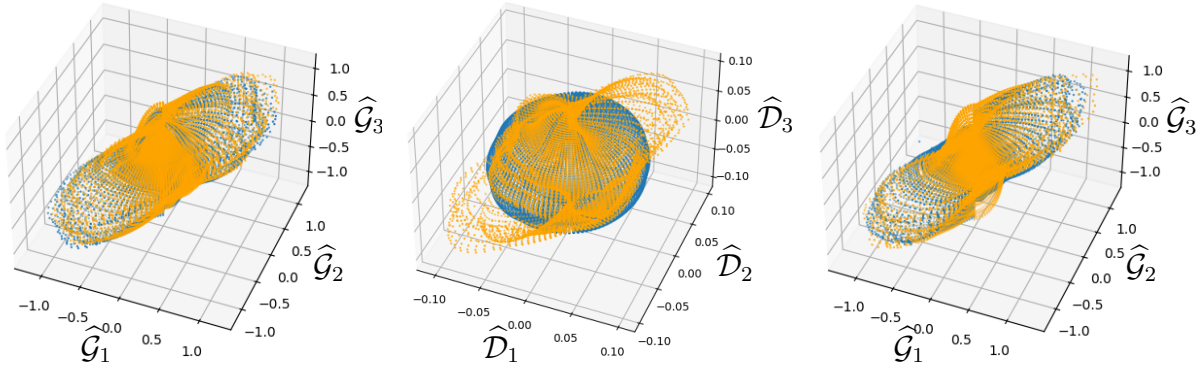


Figure 10: Estimated model parameters on 10^4 samples from a trivariate normal distribution with standard Laplace margins and the same covariance matrix as the simulation study of Section 4. *Left*: Estimated scaling set $\hat{\mathcal{G}}$ using models M_1 (orange) and M_7 (blue) with strong penalisation $\lambda_U = 100$. *Centre*: Estimated deformation sets $\hat{\mathcal{D}}$ from model M_7 with $\lambda = 100$ (blue) and with weak penalisation $\lambda = 1.0$ (orange). *Right*: Estimated scaling set $\hat{\mathcal{G}}$ using models M_2 (orange) and M_7 (blue) with weak penalisation.

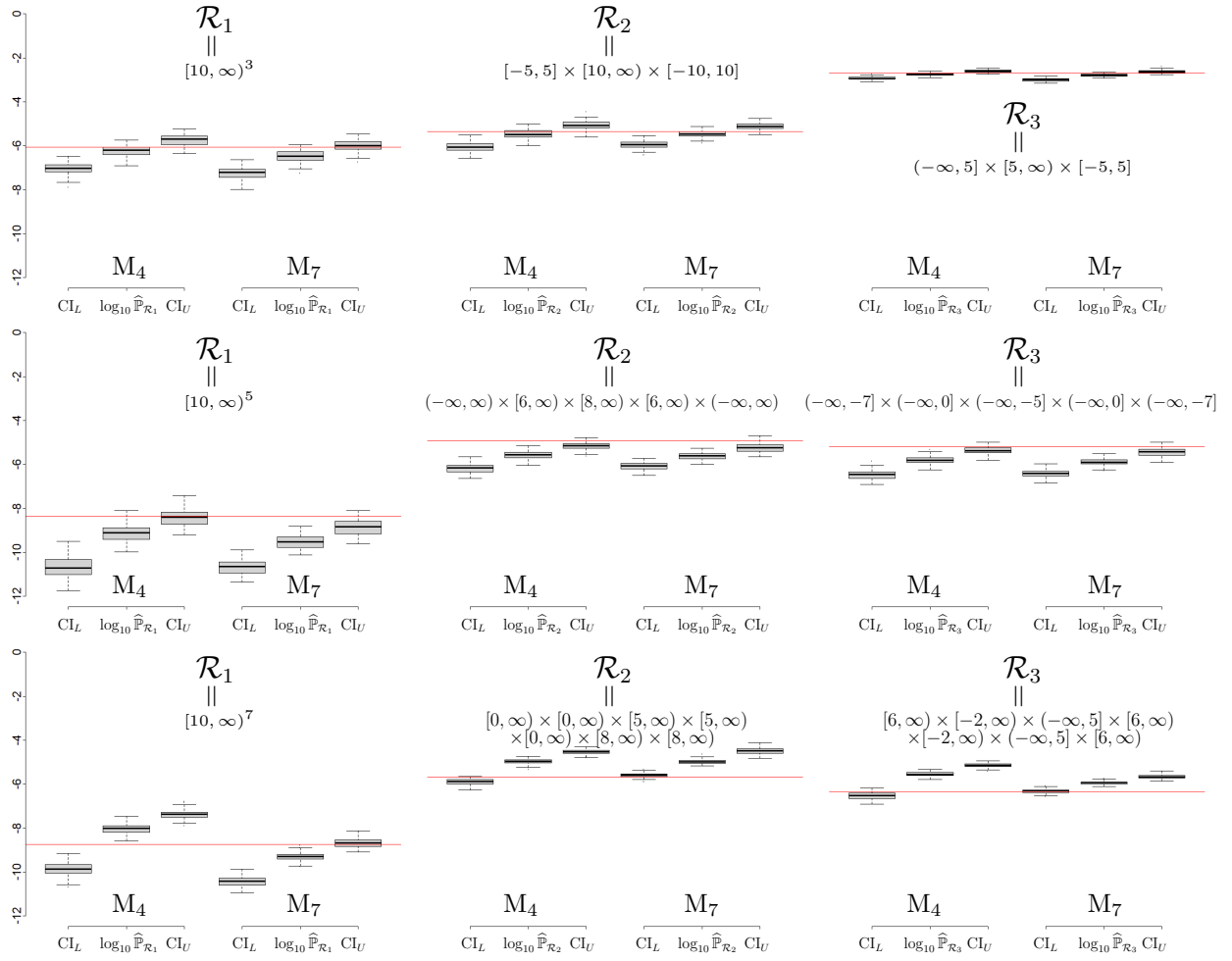


Figure 11: Boxplots of 100 estimated probabilities $\hat{\mathbb{P}}_{\mathcal{R}_j}$, $j = 1, 2, 3$, and of the lower- (CI_L) and upper-bounds (CI_U) of their 95% bootstrap confidence intervals (on log₁₀ scale) for the sets $\mathcal{R}_1, \mathcal{R}_2, \mathcal{R}_3$ using models M_4 and M_7 fitted on samples of size $n = 10^4$ from multivariate normal distributions with $d = 3$ (top row), $d = 5$ (middle row), and $d = 7$ (bottom row). The true log₁₀-probabilities are denoted by red lines.

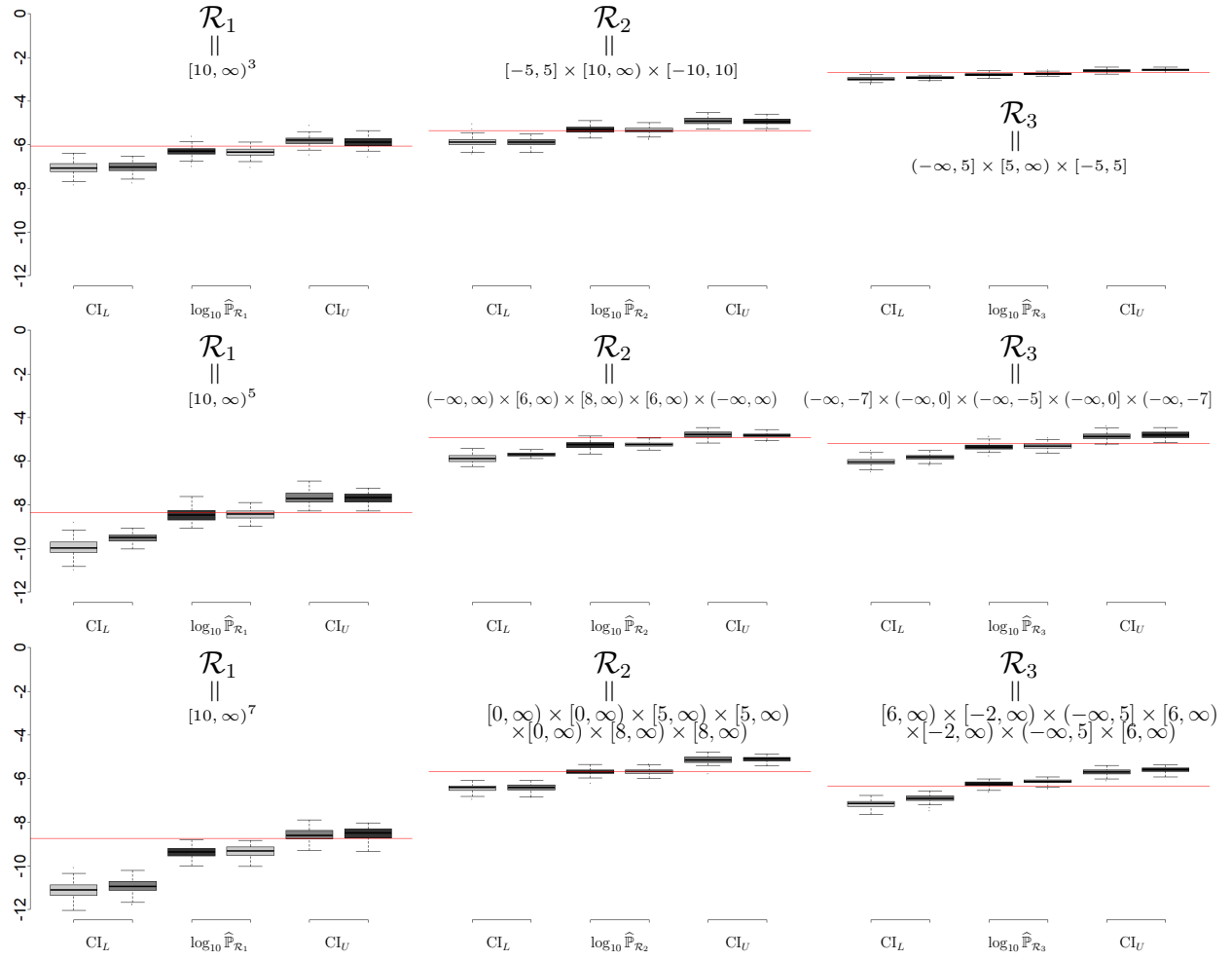


Figure 12: Boxplots of 100 estimated probabilities $\hat{\mathbb{P}}_{\mathcal{R}_j}$, $j = 1, 2, 3$, and of the lower- (CI_L) and upper-bounds (CI_U) of their 95% bootstrap confidence intervals (on \log_{10} scale) for the sets $\mathcal{R}_1, \mathcal{R}_2, \mathcal{R}_3$ using model M_2 fitted on samples of size 10^4 (light grey) and 2×10^4 (dark grey) from multivariate normal distributions with $d = 3$ (top row), $d = 5$ (middle row), and $d = 7$ (bottom row). The true \log_{10} -probabilities are denoted by red lines.

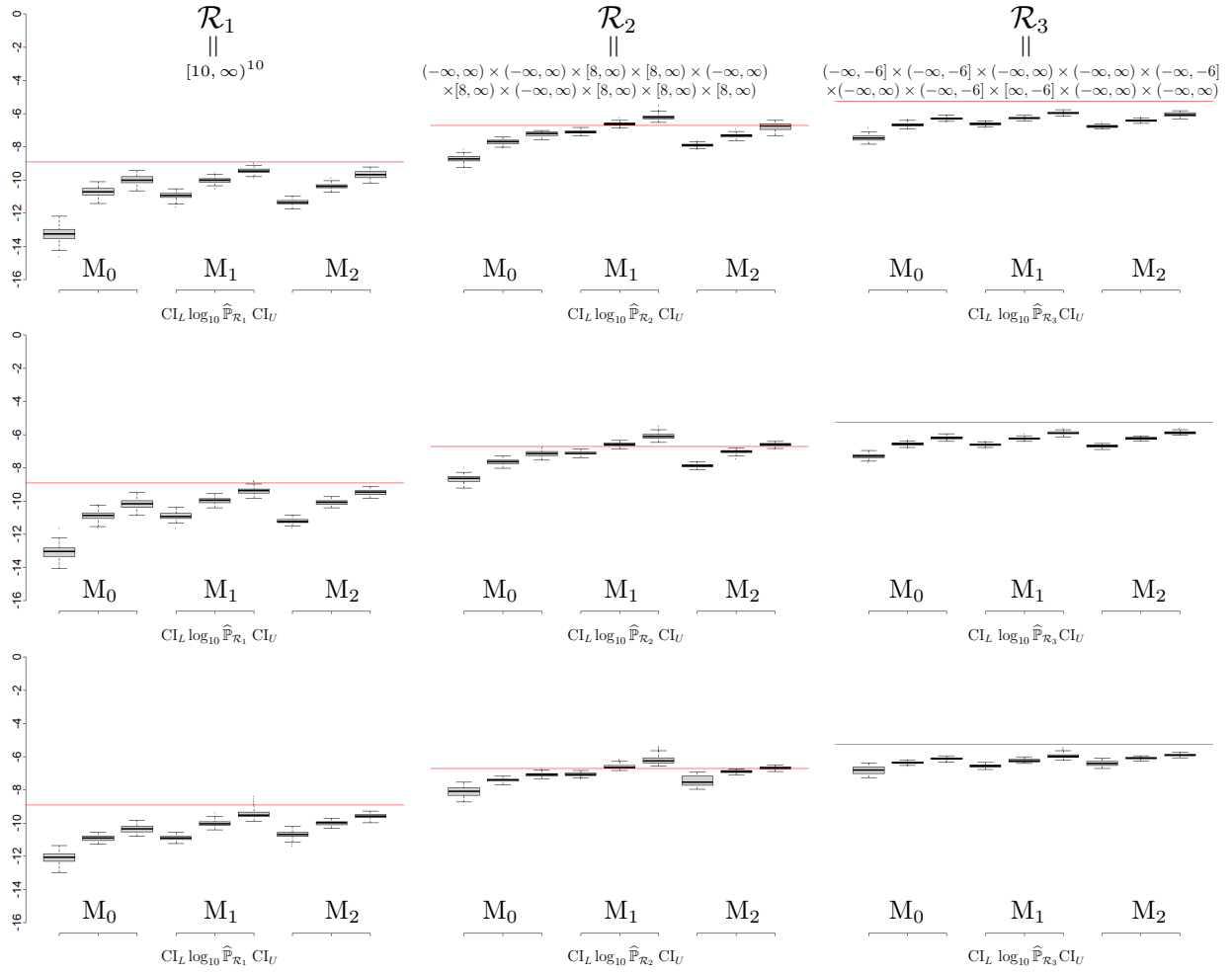


Figure 13: Boxplots of 100 estimated probabilities $\hat{\mathbb{P}}_{\mathcal{R}_j}$, $j = 1, 2, 3$, and of the lower- (CI_L) and upper-bounds (CI_U) of their 95% bootstrap confidence intervals (on \log_{10} scale) for the sets $\mathcal{R}_1, \mathcal{R}_2, \mathcal{R}_3$ using models M_0, M_1, M_2 fitted on samples of size 5×10^4 (top row), 10^5 (middle row) and 2×10^5 (bottom row) from multivariate normal distributions with $d = 10$. The true \log_{10} -probabilities are denoted by red lines.

S.9 Data application to low and high wind extremes

Table 3: Acronyms and names of the ten numbered stations with no missing data.

Number	Acronym	Name	Number	Acronym	Name
1	MEG	Megler	6	HOO	Hood River
2	NAS	Naselle Ridge	7	SHA	Shaniko
3	TIL	Tillamook	8	ROO	Roosevelt
4	FOR	Forest Grove	9	SUN	Sunnyside
5	BID	Biddle Butte	10	HOR	Horse Heaven

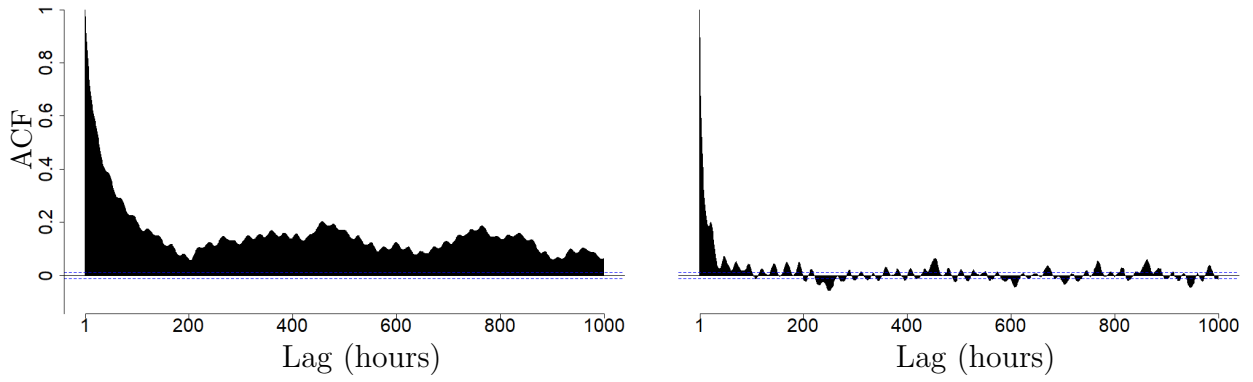


Figure 14: Autocorrelation function (ACF) plots of the original data \underline{x}_1 (left) and of the homogenised data \underline{x}_1^H (right) for site 1, MEG.

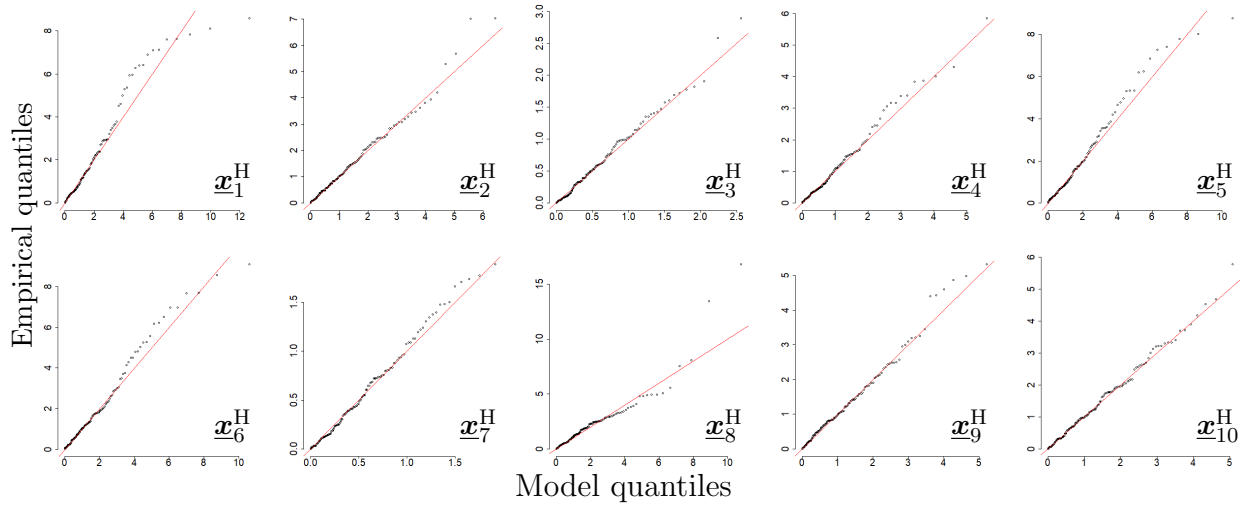


Figure 15: Quantile-Quantile plots for the marginal generalised Pareto models fitted above the 0.995-quantile of the homogenised data $\underline{x}_1^H, \dots, \underline{x}_{10}^H$.

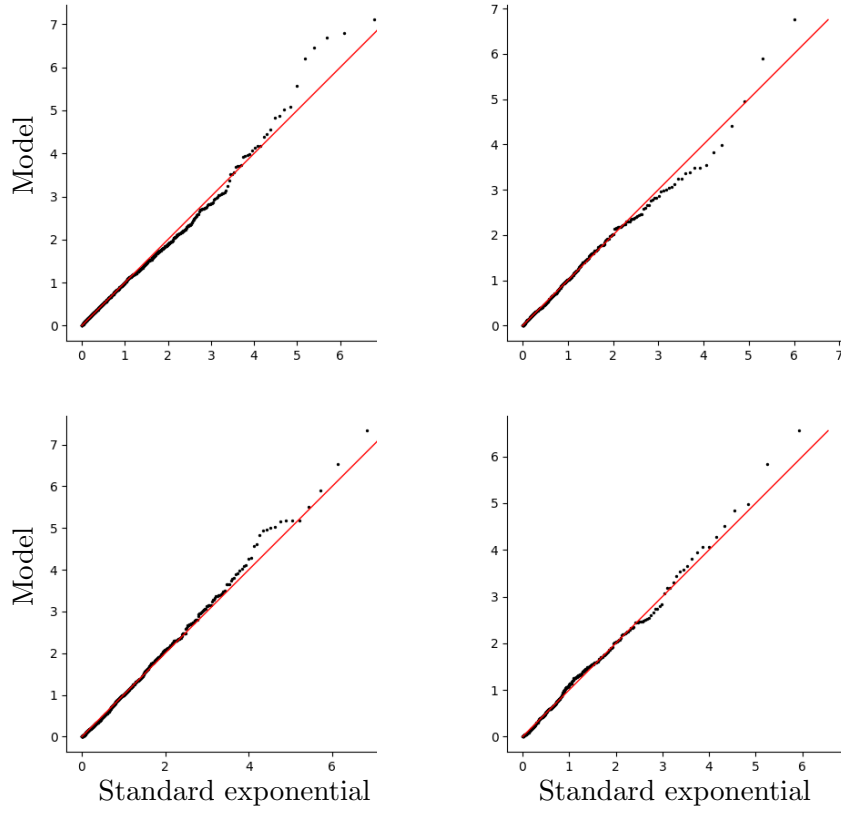


Figure 16: Quantile-Quantile plots of the standard exponential quantiles against the observed radial exceedances $\{[\|\mathbf{x}_i\| - r_{\mathcal{Q}_q}(\mathbf{x}_i/\|\mathbf{x}_i\|)]/r_{\mathcal{G}}(\mathbf{x}_i/\|\mathbf{x}_i\|) : \|\mathbf{x}_i\| > r_{\mathcal{Q}_q}(\mathbf{x}_i/\|\mathbf{x}_i\|), i = 1, \dots, n\}$ for $m = 1$ and $h = 18$ at the configuration of five stations minimising the probability of no production (top row) and maximising the probability of full power (bottom row) on their training (left column) and validation (right column) data.

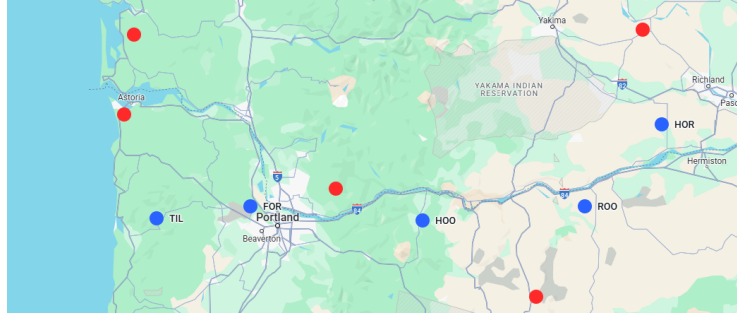


Figure 17: Configurations of five stations (blue) maximising the risk of no production for month $m = 1$ and hour $h = 18$.